GEOLOGICA CARPATHICA, DECEMBER 2020, 71, 6, 539–557 https://doi.org/10.31577/GeolCarp.71.6.5

Numerical age dating of cave sediments to quantify vertical movement at the Alpine-Carpathian transition in the Plio- and Pleistocene

STEPHANIE NEUHUBER[1,✉], LUKAS PLAN[2], SUSANNE GIER[3], ESTHER HINTERSBERGER[3], JOHANNES LACHNER[4], DENIS SCHOLZ[5], CHRISTOPHER LÜTHGENS[1], SANDRA BRAUMANN[1], FABIAN BODENLENZ[3], KLAUS VOIT[1] and MARKUS FIEBIG[1]

[1]University of Natural Ressources and Life Sciences (BOKU University), Institute of Applied Geology, Peter Jordan Straße 82, 1190 Wien, Austria; ✉stephanie.neuhuber@boku.ac.at
[2]Natural History Museum Vienna, Karst and Cave Group, Museumsplatz 1/10, 1070 Wien, Austria
[3]University of Vienna, Department for Geology, Althanstrasse 14, 1090 Wien, Austria
[4]University of Vienna, Faculty of Physics, Isotope Physics, Währinger Straße 19, 1090 Wien, Austria; present address: Helmholtz-Zentrum Dresden-Rossendorf, Bautzner Landstr 400, 01328 Dresden, Germany
[5]Johannes Gutenberg University Mainz, Institute for Geosciences, J.-J.-Becher-Weg 21, 55128 Mainz, Germany

(Manuscript received December 12, 2019; accepted in revised form November 3, 2020; Associate Editor: Michal Šujan)

Abstract: The paleoenvironmental and tectonic history at the southwestern end of the Malé Karpaty Mountains was reconstructed using sediment analysis, mineralogy, and dating. Numerical ages using $^{26}Al/^{10}Be$ burial age dating, $^{230}Th/U$ ages and luminescence age dating are combined to infer the Pliocene and Pleistocene development of the Hainburg Hills region. This study investigates sediments from two caves separated by a height difference of 92 m as well as aeolian cover sands from a fissure. The cave deposits are very unlike as one is a carbonate precipitate and the other sediment infill, but both preserve information on the uplift/incision at the Alpine-Carpathian border. Emplacement of coarse-grained fluvial deposits from the upper cave was dated to 4.1–4.6 Ma using terrestrial cosmogenic ^{26}Al and ^{10}Be in selected quartz cobbles. Calcite precipitates from the lower cave were $^{230}Th/U$ dated on three morphologically slightly different cave rafts. Ages calculated from pristine calcite are least prone to alteration and give a time of formation at ~0.31–0.34 Ma. Vertical offset rates calculated from ages and positions above the recent streambed of the Danube vary between 36–42 m/Ma for the higher position and 162 m/Ma at maximum for the lower cave and point to increased uplift/incision that has been described from other areas in the Eastern Alps and the Pannonian Basin System. Deposition of aeolian sand cover was constrained to 13.6–15.6 ka (pIRIR225 signal) and the presence of sand as opposed to its transport/erosion suggests a change in wind velocities at the Hainburg Gate. This can possibly be correlated to the termination of a cold phase with decreasing continentality accompanied by decreasing atmospheric pressure gradients. Minerals such as hematite and smectite as well as traces of poorly crystallized iron oxides found in the matrix of the upper (older) cave, were formed during warm and humid climate conditions facilitating lateritic soil formation. This is a remnant from the late Miocene or Early Pliocene soil that formed in a subtropical climate.

Keywords: burial age dating, $^{230}Th/U$ dating, uplift, Danube, cave sediment, lateritic soil, cosmogenic nuclides, isochron, Hainburg Hills.

Introduction

Fluvial sediments at elevated positions may document uplift and/or incision of an area and, if the timing of deposition can be determined, can be used to calculate rates of vertical displacement relative to the base level. Caves and their sediments are often related to the former base level and can conserve this information for long time spans. In caves, different numerical dating techniques that cover various time spans can be applied: most common is dating of speleothems using $^{230}Th/U$ dating in the precipitated carbonate but this method reaches its limit at roughly 0.5 Ma (e.g. Scholz & Hoffmann 2008). This dating method will inherently provide a minimum age of cave formation, as speleothems form after speleogenesis and possibly after a substantial lag time. Another technique that has evolved in the last two decades is burial age dating using the cosmogenic nuclide pair ^{26}Al and ^{10}Be to determine the emplacement of quartz sediments in a cave (e.g. Granger et al. 2001; Haeuselmann et al. 2007; Bella et al. 2019). This method can resolve the time interval 0.2–5 Ma. Another way to assign a numerical age to sediment deposition is luminescence dating, which is suitable for fine-grained sediments and has a temporal resolution of tens of years to ~0.5 Ma. Luminescence age dating determines the time when quartz or feldspar minerals were last exposed to daylight during sediment transport and subsequently shielded from daylight after deposition (Preusser et al. 2008; Wintle 2008; Rhodes 2011).

The Hainburg Hills form the southernmost part of the Malé Karpaty Mountains (Kleine Karpaten) located south of the present course of the Danube river. They are a prominent elevated range at the Austrian-Slovak border between the lowlands of the Vienna Basin and the Little Hungarian Plain/

Danube Lowland. So far, hints on the uplift history are given by the correlation of sediment terraces (Wessely 1961; Halouzka & Minaříková 1977) and by an intensively studied Pliocene and abundant Early Pleistocene fauna from different caves opened in a quarry (Frank & Rabeder 1997a). Up to date no attempts have been made to study the uplift of the Hainburg Hills using numerical methods. However, some attempts have been made to numerically date the incision of the Danube river and/or the mountain uplift at other locations at the Alpine-Carpathian transition to study the movement within various blocks integrated over different timespans. Apatite fission track data in exhumed crystalline rocks in the Malé Karpaty Crystalline Unit (Danišík et al. 2004) as well as $^{26}Al/^{10}Be$ burial age dating of cave sediments within the Malé Karpaty (Šujan et al. 2017) were used to calculate uplift for the larger region.

In this study, we focus on two recently excavated karst cave chambers. One cave is located 150 m above the mean water level of the Danube and 168–175 m above the base of the Danube sediments. It is filled with bright red clay and quartz cobbles. The aim of this study is to determine the timing of gravel deposition and to calculate the vertical offset rate. We use burial age dating but due to little or unknown overburden we apply the isochron technique for age calculation on seven quartz cobbles (Balco & Rovey 2008). In addition, we use $^{230}Th/U$-dating of cave rafts in a second cave located 92 m below the cave chamber filled with red matrix and quartz gravel as a second tie point to determine vertical movement relative to the base level. Our results are compared with previously published uplift/incision rates and to age ranges of fossil findings from the closer vicinity and similar heights (Frank & Rabeder 1997a). A second issue is the investigation of paleoclimatic conditions using matrix minerals. Numerical dating in combination with paleoenvironmental evidence is used to establish a sequence of sediment accumulation events to reconstruct the Pliocene and Pleistocene history of the Hainburg Hills.

Study area

The Vienna Basin developed in the Neogene (predominantly Miocene) at the transition of the Eastern Alps and the Western Carpathians and is filled with mainly marine and to a lesser extent, lacustrine sediments (Strauss et al. 2006; Fig. 1). Its eastern border northeast of the Lower Austroalpine Leitha mountains is formed by the Malé Karpaty and the Hainburg Hills that consist of a Paleozoic magmatic and metamorphic basement and Mesozoic cover sediments. East of this dissected hilly range, the Danube Basin (Kisalföld or Little Hungarian Plain) also formed during the Miocene (Sztanó et al. 2016). The Danube Basin is a part of the Pannonian Basin System and is separated from the Great Hungarian Plain by another uplifted basement high zone, the Transdanubian Range (Fig. 1a).

The Hainburg Hills form a 10 km-long E-W-oriented ridge and several smaller hills with the highest elevation at the Hundsheimer Berg (480 m; Fig. 2) and separate the Vienna Basin from the Danube Basin. As part of the Internal Western Carpathians they consist of (base to top) Variscan magmatic and metamorphic rocks (Bratislava granodiorite intrusion age: 351–355 Ma, Uher et al. 2014) covered by Mesozoic sediments, mainly Middle Triassic carbonates (Wessely 1961). The Alpine orogeny led to a low-grade metamorphism and subsequent exhumation. During the Miocene, predominantly marine sediments were deposited. In the late Miocene (Pannonian) the environment shifted to lacustrine, deltaic, and fluvial conditions. Fluvial deposits that often contain coarse gravels dominate in the Plio- and Pleistocene. The paleo-Danube river had its main channel south of the Hainburg Hills and the change to its present (i.e. northern) position occurred presumably during the Middle Pleistocene (Wessely 1961; Zámolyi et al. 2017; Šujan et al. 2018).

The Hainburg Hills mark the edge of two basins with different sediment accommodation spaces. Quaternary sediments to the west, in the central Vienna Basin directly south of the Danube are very thin with a maximum thickness of 10 m overlying late Miocene sediments (Fig. 1b). As summarized by Salcher et al. (2012) farther to the south, those sediments may reach up to 175 m (Mitterndorf Basin, MB, Fig. 1) or 90 m (Lassee Depression, LD, Fig. 1), Obersiebenbrunn Depression, Aderklaa Depression) north of the Danube. In comparison, Quaternary sediments in the Danube Basin may reach over 400 m in its central part (e.g. Šujan et al. 2018). In contrast to the Vienna Basin, Quaternary sediments east of the Hainburg Hills are little affected by tectonic displacement.

Bad Deutsch-Altenburg is a village at the western margin of the Hainburg Hills that is known for its thermal sulfuric spa since Roman times. The village is located at the Danube river with a present average water level at about 140 m a.s.l. and a water depth of 2 to 5 m. Sediment thickness upstream of the Hainburg Gate is estimated to 7–15 m a.s.l. (Zottl & Erber 2003) and accordingly the base of the Danube sediments is estimated between 131 and 120 m a.s.l.

25 karst caves have been documented at the western and southern slope of the Hundsheimer Berg and Spitzerberg. All caves show signs of a hypogenic speleogenesis and almost all were discovered during quarrying (Plan & Spötl 2016; Spötl et al. 2017). The elevations of the caves range from 142 to 310 m a.s.l. While most caves show signs of a hydrothermal origin, the morphology of the ones north of Bad Deutsch-Altenburg reveal sulphuric acid speleogenesis (De Waele et al. 2016). East of this village an impressive quarry covers an area of c. 0.5 km² and exposes rock from 190 m a.s.l. to the former summit of Pfaffenberg at 331 m a.s.l., that has been removed by open-pit mining. Mining activity in the Hollitzer quarry (named after its first owner) dates back to 1906. Extracted lithologies are Middle Triassic dolomite and limestone as well as Jurassic carbonate breccia (Wessely 2006). Miocene Leitha limestones (Badenian Stage/Langhian to early Serravalian) as well as conglomerates, sandstones and marls (Sarmatian/late Serravalian) partly cover these rocks in the south and east.

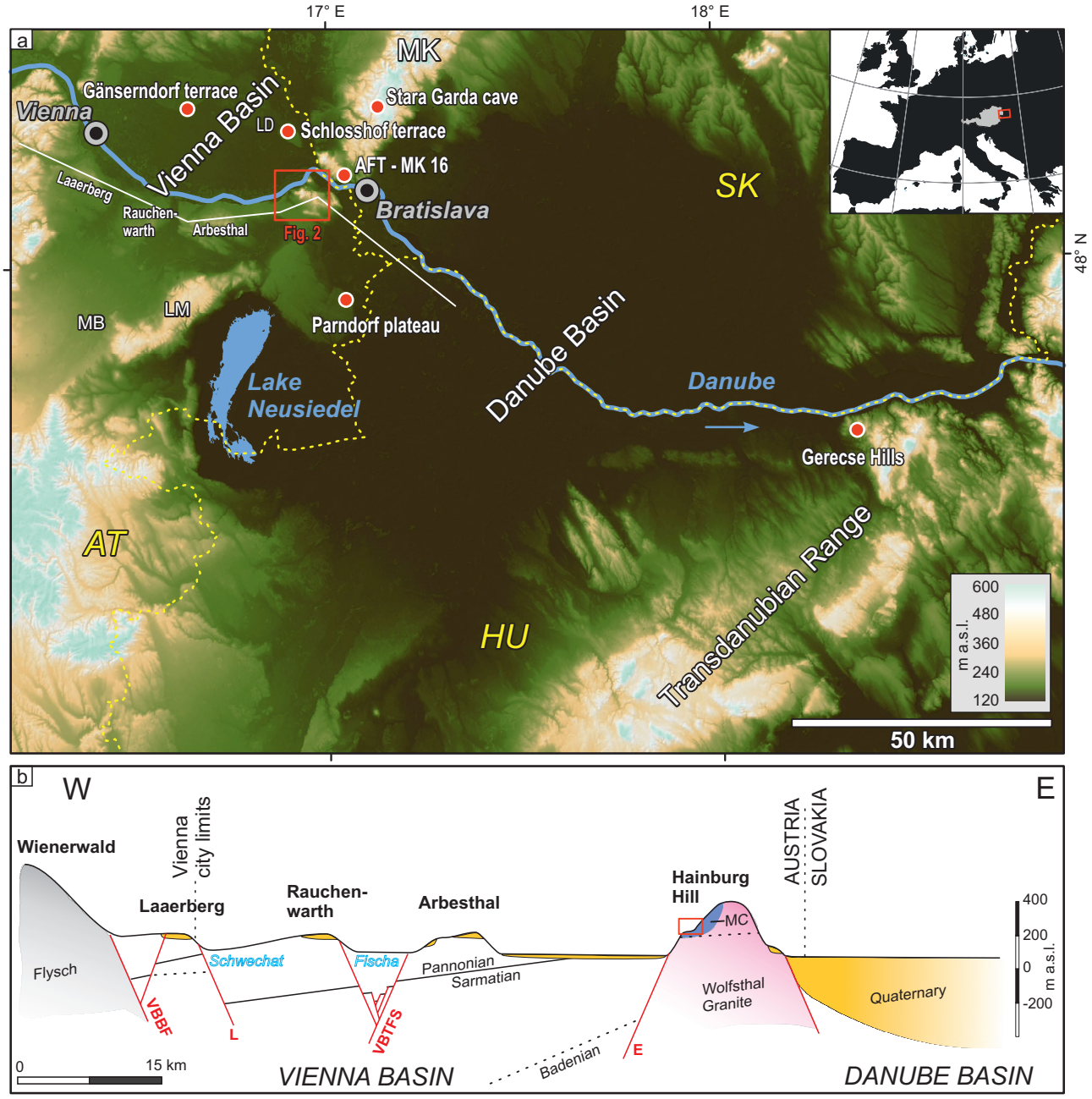

Fig. 1. a — Overview of the Alpine-Carpathian-transition including locations mentioned in the text. LM: Leitha mountains, MK: Malé Karpaty; LD: Lassee Depression; MB: Mitterndorf Basin. Background: shaded DEM (courtesy EU, Copernicus); White line: profile trace for 1b; Inset upper right shows the map extent with respect to Austria. **b** — Schematic W-E-section following trace in 1a (simplified and compiled from Fuchs 1986a, b; Wessely 2006; Salcher et al. 2012; Šujan et al. 2018) through the central Vienna Basin south of the Danube via Hainburg Hills into the Danube Basin; Sarmatian-Pannonian boundary is indicated by solid black line and is cropping out (dashed line=base Sarmatian) at Hainburg Hills with only Sarmatian deposits; VBBF: Vienna Basin Boundary Fault (Sollenau fault), L: Leopoldsdorf Fault; VBTFS: Vienna Basin Transform Fault System; E: Engelhartstetten Fault; MC: Mesozoic Carbonate; red rectangle: sampling position at Hainburg Hills.

At the top, fine-grained, loess-like aeolian sediments with a thickness of up to a few meters are cropping out.

In 1908, a first cave containing a rich fossil vertebrate fauna was discovered. Subsequently, a total of 51 smaller and larger fossil bearing karst cavities were opened during quarrying (Mais & Rabeder 1977; Frank & Rabeder 1997a and references therein). Most of the caves were sediment-filled and progressive mining revealed a connection between the caves in many cases. Most of the fauna is of Early Pleistocene age and was found in cavities between 233 and 312 m a.s.l. It comprises molluscs, amphibians, reptiles, aves, and mammals and is considered as important assemblage for this period for Central Europe (Maul & Markova 2007; Nadachowski et al. 2011; Garcia-Ibaibarriaga et al. 2015). Middle Pleistocene

fossils – mainly large mammals – are restricted to one low-lying cave (205 m a.s.l., Frank & Rabeder 1997a). Only some unroofed cavities ("Spalten" sensu Frank & Rabeder 1997a) in the uppermost part (285 to 312 m a.s.l.) contained fossils of the "Gilesian stage" – this corresponds to the late Pliocene (Piacenzian, 2.58 to 3.60 Ma) according to the current stratigraphic table (Cohen et al. 2013) and middle Pliocene according to the old one used by Frank & Rabeder (1997a). All of these *Spalten* were completely filled by a reddish soil ("terra rossa") that partly contained gravels.

During the last decade six caves were accessible in the Hollitzer quarry at elevations between 199 and 293 m a.s.l. (Plan 2019). The longest is Hollitzerhöhle III with a length of 117 m. All caves have cupola morphologies and other signs of a hydrothermal origin probably under phreatic conditions. Neither thick deposits of clastic sediments nor fossil-bearing layers are present, but most of the caves contain cave popcorn and two of them cave rafts. The latter are thin flakes of carbonate that form at the surface of cave pools due to evaporation (Hill & Forti 1997) and eventually sink to the ground when they become too heavy or are hit by dripping water. Due to the thermal gradient between water and cave air, they are abundant in hydrothermal caves (e.g. Szemlő-hegyi and József-hegyi Caves in Budapest; Szanyi et al. 2012).

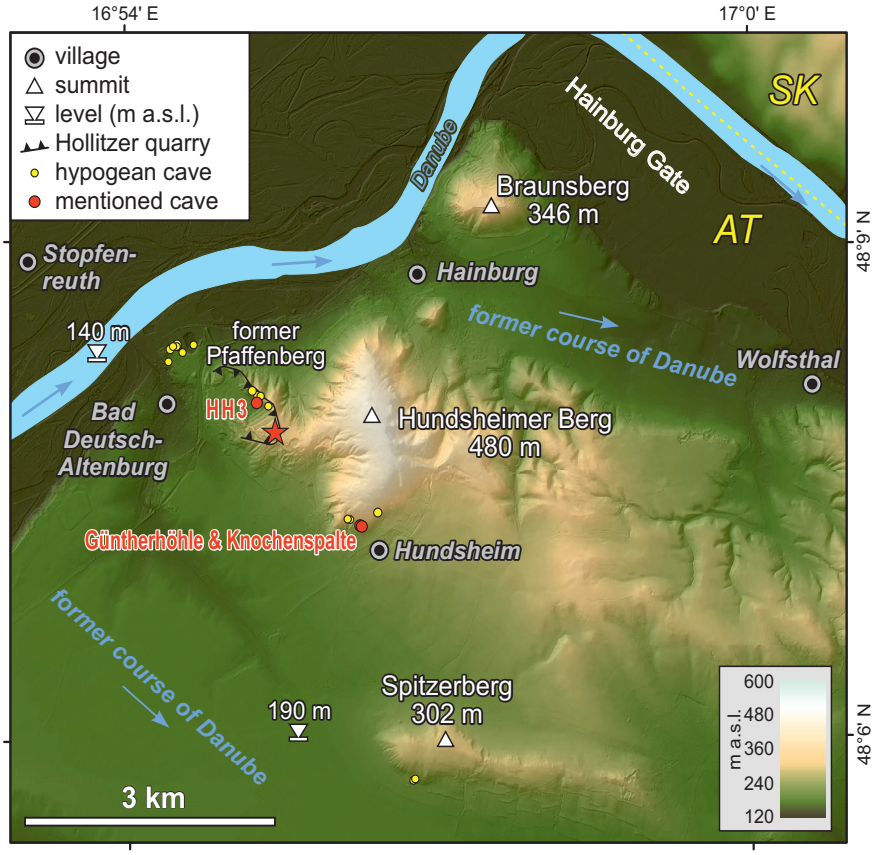

Fig. 2. The Hainburg Hills. Danube main channel N of Braunsberg. The red star marks the filled cavity (samples HOL3, Figs. 3e,f, 4). HH3: Hollitzerhöhle III. Background shaded ALS-DEM (courtesy Land Niederösterreich).

Field observations and sampling

In February 2015, the excavation of a large soft sediment outcrop that contained quartz pebbles was reported from the Hollitzer quarry. The quarry was successively visited during three stages of excavation. On 25/2/2015, a 15 to 20 m wide and at least 20 m high cave chamber, filled with large well-rounded quartz cobbles in a flashy red matrix was exposed (Fig. 3a,c). The sedimentary fill was mostly matrix supported with no observable sorting or sedimentary structure. The cave ranged from quarry level 280 to 300 m a.s.l. (WGS84 48.131101°N, 16.922994°E) and was open towards the upper level. The cave walls were exposed and showed undulating round and occasionally cupola-like corrosional morphologies. Some parts were coated by a millimeter-thick layer of flowstone. As the surface has spherical morphology similar to cave clouds, that form under phreatic conditions, it seems likely that this cave also formed under such conditions. Seven large quartz cobbles (HOL3) from the same height were sampled for $^{26}Al/^{10}Be$ burial age dating from the sediment of this chamber at 290 m a.s.l. (Fig. 3f).

At the top of the quarry within pockets of the karstic bedrock surface (Fig. 4), cavities open to the surface were also filled with coarse cobbles. Only the uppermost cover of the void consisted of well-sorted fine sands. Based on lamination and uniform grain size, those sediments were identified as *in-situ* and most likely of aeolian origin. Wind transported sediments guarantee sufficient light exposure of mineral grains before deposition to fully reset the luminescence clock by optical bleaching and are particularly suitable for the application of optical dating techniques. Two samples were taken from different pockets in light tight stainless-steel tubes (see Fig. 3d), with sample HOL1 at an altitude of c. 310 m a.s.l. and sample HOL2 in a position c. 5 m higher. Sediment in direct contact to each luminescence sampling spot was taken for determination of the natural background radiation using high resolution, low-level gamma spectrometry.

During a second visit (21/11/2016) this chamber and its fill had been largely removed. We estimate from field observation

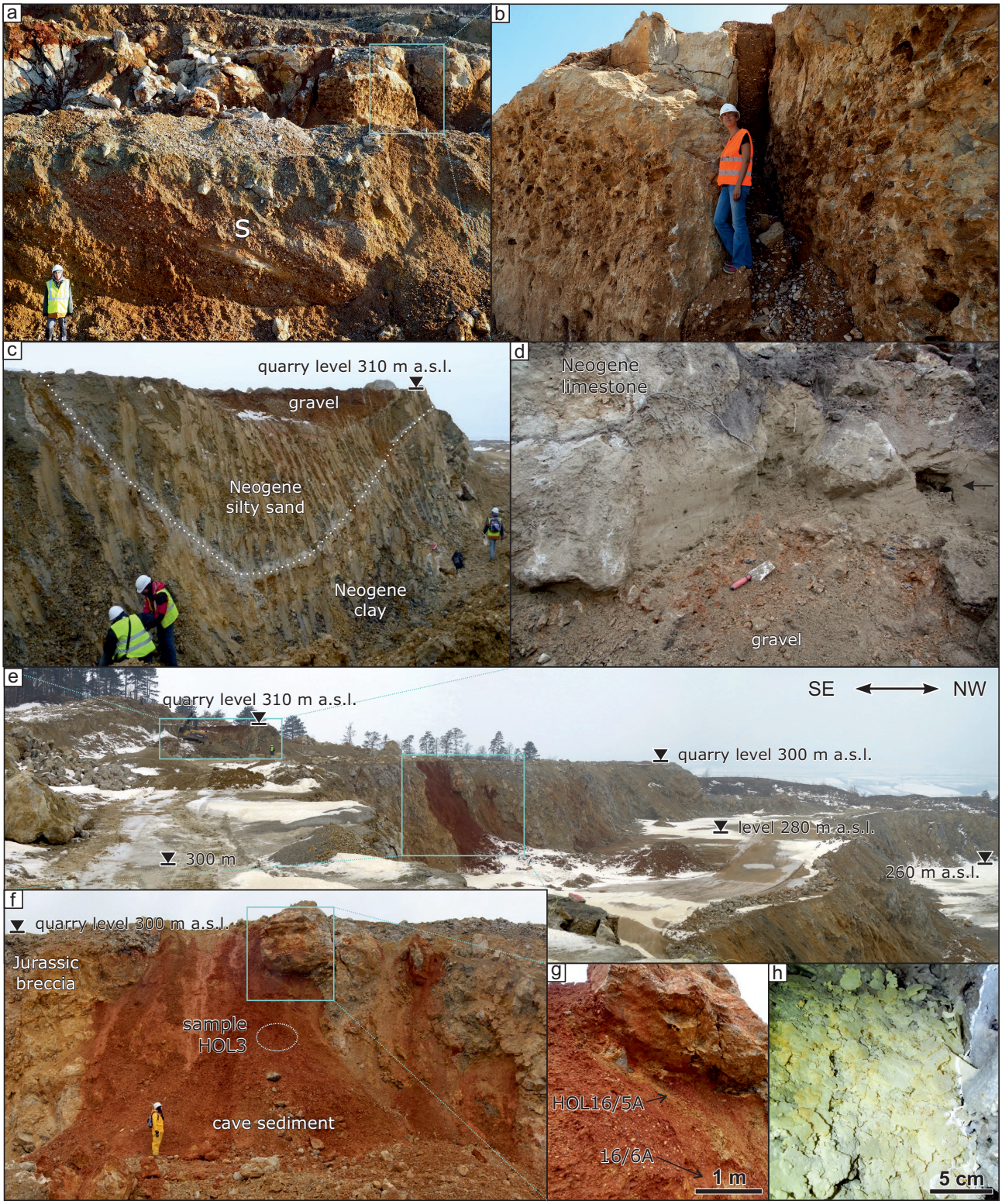

Fig. 3. Outcrop photographs: **a** — Gravels and sand lens (below "s") in the foreground; heavily corroded hostrock (Neogene conglomerate) filled with gravels on 21/11/2016; **b** — Detail of corroded walls and sediment fill; **c** — Uppermost part of the stratigraphic sequence with quartz-rich gravel on top; **d** — Consolidated Neogene conglomerate in contact with fluvial gravel overlain by aeolian sediment; top black layer is humus cover; Luminescence sampling point (arrow) right part of picture; **e** — Overview of the southeastern part of the Hollitzer quarry on 25/2/2015; **f** — Sediment filled cave chamber (sample HOL3); **g** — Detail of quartz bearing sediment fill and corrosional cave wall morphology and position of matrix samples HOL16/5A and 16/6A; **h** — Yellowish cave rafts in Hollitzerhöhle III; the ones in the foreground show a coralloid calcite overgrowth; the ones in the background almost none.

that the chamber covered an area of c. 20 × >10 m and was more than 20 m high with a volume of >4000 m³. During this visit, sediments with similar sedimentary facies (i.e. red matrix and large quartz cobbles) were exposed at 280 and 300 m a.s.l. and were sampled for granulometry and mineralogical investigation (samples HOL16/3A, 16/3B, 16/3C, 16/3D, 16/5A and 16/6A, see Fig. 4). At the top level of the quarry the gravel formed a body with concave erosional contact to the Neogene rock below (Fig. 3c) and contained – apart from abundant quartz – few clasts of intensely weathered magmatic and metamorphic rocks that disintegrated on touch. The cobbles long axes were dipping towards south with foresets in the same direction (Fig 3a). Within the sediment body one sand lens was exposed and sampled for mineralogy and heavy mineral analysis (sample HOL16/3B, Table 1).

On 9/8/2017, an impressive fault with partly polished slickensides was exposed with at least 50 m length and 15 m height above the 280 m a.s.l. quarry level. It was located 50 m ENE (hill-wards) from the former sediment filled cave (WGS84 48.131269°N, 16.923672°E). The fault plane was dipping west (267/45) and another possibly first generation of lineation with wide and deep scratches was dipping 325/55 with a dextral/normal shear sense. A less prominent probably younger lineation showed a pure dip slip normal direction. The fault cut through Miocene (probably Sarmatian) conglomerates.

In the uppermost part of the quarry (c. 310 m a.s.l.), where vegetation was freshly removed, a network of at least 3 m-deep and 0.5 to 1 m-wide vertical fissures was exposed (Fig. 3e, f). They were filled with quartz cobbles in a red matrix similar to the previously found cave sediment. The walls of the conglomerate towers in between showed a striking corrosive morphology with abundant decimeter-wide pockets. The pockets resembled dissolved clasts and some of them showed lithophaga-endocasts that projected into the holes.

During that visit, cave rafts were collected from an ascending gallery in Hollitzerhöhle III at 198 m a.s.l. (Fig. 3g). Most cave rafts were coated by younger coralloid calcite layers, but in one small, tube-shaped niche we found thin, sharp edged, and uncoated cave rafts (HH3-2). Samples from another niche close by to the left were slightly more overgrown (HH3-3) and a third sample from an inclined wall had a significant amount of coating (HH3-1).

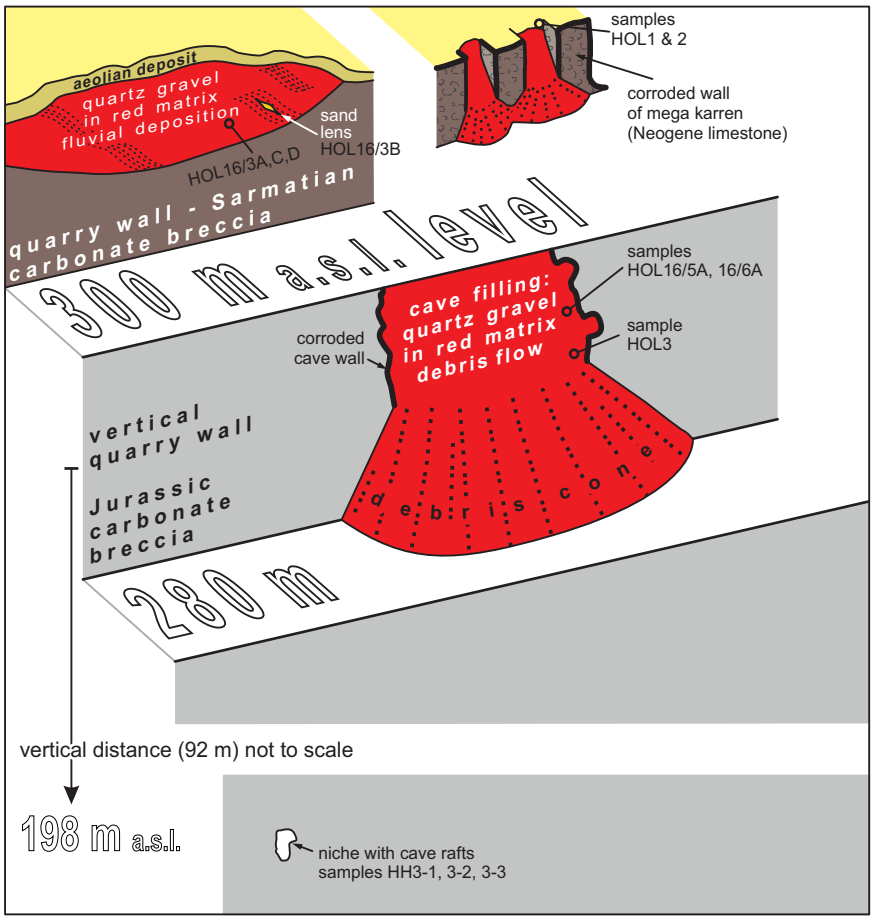

Fig. 4. Sketch of the outcrop situation and sampling points – synthesis of three visits between Feb. 2015 and Aug. 2017. Compare also to overview in Fig. 3e.

Methods

Granulometry

Prior to grain size analysis, the samples were treated with 15 % hydrogen peroxide to remove organic matter and later disintegrated by treatment with a 400 W ultrasonic probe for 3 min. A sandy sample (HOL16/3B) was wet-sieved (sieve mesh sizes: 2; 1; 0.5; 0.25; 0.125; 0.063 mm) and the fraction <63 µm to 0.2 µm was analyzed using a SediGraph 5100 (Micromeritics) together with two red, fine-grained samples (HOL16/5A and HOL16/6A).

Pebble counting, bulk- and clay mineralogy

The gravel sample HOL16/3A was dry-sieved using mesh sizes of 64, 32, 16 and 8 mm. The components were washed

Table 1: Sample locations within the quarry, analyses and results of X-ray diffraction (XRD) and clay mineral analysis.

sample		location	sample description	analyses		results		
					grain size	XRD	clay mineralogy	IR+STA
HOL1		level 310	unconsolidated sandy sediment	luminescence age dating	x			
HOL2		level 310	unconsolidated sandy sediment	luminescence age dating	x			
HOL16/3	**A**	level 300	gravel/red matrix	pebble counting: quartz, quartzite	x			
	B		sand lens	heavy mineral analysis	x		illite, kaolinite, smectite, traces of mixed layer clay minerals, natrojarosite, natroalunite, birnessite	
	C		matrix of A		x	quartz, microcline, muscovite, chlorite, hematite		iron oxides, traces smectite
	D		weathered component in A			quartz, microcline, muscovite, kaolinite		
HOL3	**1 to 7**	wall at c. 293 m	7 quartz cobbles	burial age dating				
HOL16/5A		Above level 280	brown matrix		x	quartz, microcline, muscovite, smectite, kaolinite, goethite	53 % smectite, 33 % illlite, 14 % kaolinite	
HOL16/6A		Above level 280	redish brown matrix		x	quartz, microcline, muscovite, smectite, kaolinite	58 % smectite, 25 % illlite, 16 % kaolinite	
HH 3	**1 to 3**	level 198	3 cave rafts	^{230}Th/U age dating				

and the lithology of the different size fractions was determined. Mineralogical composition of the finer samples was established using X-ray diffraction (XRD) with a Panalytical X'Pert PRO diffractometer (Cu Kα radiation, 40 kV, 40 mA, step size 0.0167, 5 s per step) at the Department of Geology, University of Vienna. The samples were loaded in sample holders as oriented powder. X-ray diffraction patterns were interpreted using the Panalytical software "X´Pert High score plus". The bulk mineralogy of samples HOL16/3C, 16/3D, 16/5A, 16/6A was determined. Additionally, the clay fraction of samples HOL16/3B, 16/5A and 16/6A was separated and analyzed.

For clay mineral analysis, the samples were first disaggregated with diluted hydrogen peroxide to remove the organic matter and subsequently treated with a 400 W ultrasonic probe for 3 min. The <2 µm-fraction was separated in an Atterberg cylinder, where the suspension was drained after a settling time of 24 h 33 min (formula after Stokes, from Köster 1964) and dried at 60 °C. Oriented clay samples were prepared by pipetting the suspensions (10 mg sample in 1 ml of distilled water) onto glass slides and air dried. Oriented XRD mounts were analyzed saturated with Mg and K ions, and after saturation with ethylene glycol and glycerol at 60 °C for 12 h. The saturation with ethylene glycol and glycerol was carried out to identify expandable clay minerals like smectite and vermiculite (Moore & Reynolds 1997). Additionally, the samples were heated to 550 °C to destroy kaolinite and expandable clay minerals (Moore & Reynolds 1997). The relative amount of clay minerals in the clay fraction was quantified using correction factors of Schultz (1964).

Simultaneous thermal analysis

Simultaneous thermal analysis (STA) uses weight loss of endothermic and exothermic reactions to identify mineral phases, organic carbon, and amorphous phases. 50 mg of sample was heated to 1000 °C in a Netzsch STA 409PC LUXX® with gas control PU1.851.06 using a 50 ml/min air and 15 ml/min N_2 gas flux rate and a temperature increase of 10 °C/min. Results were quantified according to different reaction temperatures using the built-in software at the Institute of Applied Geology (BOKU University, Vienna).

Infrared spectroscopy

To identify amorphous constituents, we used the Bruker Tensor 27 IR Spectrometer at the Clay Mineralogy Laboratory of the Institute of Applied Geology (BOKU University,

Vienna). Powdered samples were dried (80 °C) overnight and cooled in a desiccator to remove interference by adsorbed water. 1 mg of dried powder mixed with KBr was pressed (15 Kbar) for measurement.

Heavy mineral analysis

Heavy minerals from one sand lens (HOL16/3B) were separated from the fractions 125–250 µm and 63–125 µm using LST Fastfloat at a density of 2.95 g/cm³. The heavy fraction was embedded in Canada balsam and inspected using polarized light.

^{26}Al/^{10}Be burial age dating

The radioactive decay of *in-situ* (in quartz) produced cosmogenic ^{10}Be and ^{26}Al is used to calculate the duration of shielding from cosmic radiation and hence to determine the time of sediment burial. A typical example is exposed sediment washed into a cave where it is completely shielded from cosmic radiation (Granger & Fabel 2019). In this buried sample, the initial ratio of ^{26}Al to ^{10}Be equals the surface production rate ratio P_{26}/P_{10} (6.8 ± 0.5; Zhao et al. 2016) that decreases with increasing burial duration according to the half-life of each nuclide.

Sediments affected by more complex burial and exposure histories may bring decreased initial ratios to their current position. One way to exclude those problematic samples is the isochron method (Balco & Rovey 2008). It is applied to samples that share the last depositional event and post-burial history but have different nuclide concentrations due to different production- and denudation rates in their individual source areas. In addition, using the isochron method, post-burial nuclide production due to shallow burial depth can be neglected, as it is constant for all samples taken from the same burial depth. The samples fulfilling the above presumption plot along a line in an ^{26}Al vs. ^{10}Be diagram. Samples that do not follow a linear trend can be identified and must be excluded because they contain a burial signal, which is not consistent with the rest of the samples, i.e. the signal does not reflect the last, shared burial event.

At our study site the overburden is missing today. Comparison with old maps indicates 15 to 20 m cover thickness prior to quarrying, which is a relevant depth for post-burial production, especially in old sediments (Braucher et al. 2013; Granger 2014). Therefore, we use the isochron method for numerical age calculation.

Cosmogenic ^{10}Be and ^{26}Al nuclides of seven clasts sampled at the same depth and thus subject to the same post-burial history were extracted using the procedure developed at PRIME Lab (Purdue University, USA, Granger et al. 2001; Gibbon et al. 2009; Zhao et al. 2016) at the Geochemistry Department of the Austrian Geological Survey (Vienna) and at the Laboratory for Cosmogenic Nuclide Extraction at the Institute of Applied Geology (BOKU University, Vienna). Aluminum and beryllium oxides were analyzed at the VERA facility (Isotope Research, University of Vienna) (Steier et al. 2019) and calibrated using secondary standards. For Aluminum measurements, two reference materials were used: "Purdue-2" with an ^{26}Al/^{27}Al ratio of 2.71 ± 0.02^{-12} and "Purdue-3" with a ratio of 3.55 ± 0.05^{-12} (Wallner et al. 2000). For Beryllium, we used the secondary standard SMD-Be-12 (calibrated to NIST 4325) with a ^{10}Be/^{9}Be ratio of 1.704 ± 0.03^{-12} (Akhmadaliev et al. 2013). ICP-OES (Perklin Optima 8300, at the Institute of Forest Ecology, BOKU University, Vienna) was used to determine total Aluminum in sample aliquots. Total uncertainties on ^{10}Be and ^{26}Al concentrations are combined AMS measurement error, uncertainties on the nuclides' production rate ratio, uncertainties on the nuclides half-lives and ICP-OES errors for Aluminum calculated by error propagation.

Samples for ^{10}Be and ^{26}Al analysis were prepared in three batches (b6, b8, b9; Tables 2 and 3). A blank correction of subtracting the blank ratio from the ratios of the samples was performed for all ^{26}Al measurements and for batches b6 and b8 for ^{10}Be. The samples and the blank for ^{10}Be of batch b9 gave particularly low and unstable currents that resulted in large uncertainties. The count rate on the blank of this batch was rather high. For batch b9 the blank count rate (3 events per minute) was subtracted from the samples' count rates (3–10 events per minute).

The age was computed using a MATLAB script (Granger 2014) described by Braumann et al. (2019). The parameters and used constants are summarized in Table 4. To quantify age uncertainties, a Monte-Carlo simulation with 10,000 runs based on recursive fits of ^{26}Al and ^{10}Be data was performed assuming an initial ratio of ^{26}Al/^{10}Be=6.8. To account for the variability in the initial ratio of ^{26}Al/^{10}Be the end-members (6.3/7.3, Table 1) were also used in additional runs. At the beginning of each run, random ^{26}Al and ^{10}Be values within the measured error bars were picked based on a Gaussian fit. The original script was updated regarding the random selection of errors for ^{26}Al and ^{10}Be values to ensure a complete coverage of the measurement error interval.

^{230}Th/U dating of cave rafts

Sample preparation and analysis were performed at the Max Planck Institute for Chemistry, Mainz, Germany, using a Nu Plasma MC-ICPMS. The samples were weighed, dissolved in 7N HNO_3, and spiked with a mixed ^{229}Th–^{233}U–^{236}U-solution. Details on the calibration of the spike are given in Gibert et al. (2016). The samples were then evaporated and treated with a mixture of concentrated HNO_3, HCl and H_2O_2 to destroy potential organic material. Then, the samples were dried, re-dissolved in 6N HCl, and U and Th were separated using ion exchange columns (see Yang et al. 2015 for details). A detailed description of the MC-ICPMS procedures is given by Obert et al. (2016). All activity ratios were calculated using the decay constants of Cheng et al. (2000) and corrected for detrital Th assuming a bulk Earth ^{232}Th/^{238}U

Table 2: Analytical Be data; the samples were processed in three different batches (b6, b8, b9), the associated process blanks are given at the base of this table; all ^{10}Be concentrations are corrected for process blanks. A home-made carrier following Stone (1998) from a deeply mined beryl was used with ^{9}Be=6,645±133 mg/kg and ^{10}Be/^{9}Be=0.93±0.3 · 10^{-15}.

sample	#	quartz	mass ^{9}Be from carrier	^{10}Be/^{9}Be	^{10}Be/^{9}Be err.	^{10}Be	err ^{10}Be
	batch	[g]	[mg]	[-]	[%]	[atoms/g Q]	[%]
HOL3-1	b9	30.15	0.1683	8.80E−13	40.9	328,199	42.4
HOL3-2	b9	64.72	0.1526	7.50E−13	13.3	118,204	17.4
HOL3-3	b6	70.42	0.2737	9.55E−14	3.5	24,821	11.7
HOL3-4	b9	20.41	0.1443	2.00E−14	100.0	9,447	100.6
HOL3-5	b8	50.29	0.3435	1.18E−13	3.6	53,600	11.8
HOL3-6	b9	27.09	0.1720	8.00E−14	87.5	33,931	88.2
HOL3-7	b9	50.95	0.1523	1.50E−13	6.7	29,970	13.0
blank b6	b6	n.a.	0.2637	3.80E−15	15.79	n.a.	19.34
blank b8	b8	n.a.	0.4422	3.27E−15	23.86	n.a.	26.35
blank b9	b9	n.a.	0.1557	The blank gave very low currents and a count rate of c. 1 event in 20 seconds. This rate was subtracted from the samples' count rates as blank correction.			

Table 3: Analytical Al data; the samples were processed in three different batches (b6, b8, b9), the associated process blanks are given at the base of this table; all ^{26}Al concentrations are corrected for process blanks. A Merck certipur carrier was used with ^{27}Al=984±5 mg/kg (derived from NIST SRM 3101a).

sample	#	quartz	mass ^{27}Al from carrier	^{27}Al total (ICP- OES)	^{27}Al err (ICP-OES)	^{26}Al/^{27}Al	^{26}Al/^{27}Al err	^{26}Al	^{26}Al/^{10}Be	err^{26}Al/^{10}Be
	batch	[g]	[mg]	[mg]	[%]	[-]	[%]	[atoms/g Q]	[-]	[%]
HOL3-1	b9	30.15	1.2768	1.71	0.03	1.53E−13	5.2	190,917	0.582	41.3
HOL3-2	b9	64.72	0.8767	2.02	0.02	2.550E−13	4.7	176,473	1.493	11.1
HOL3-3	b6	70.42	1.2379	1.99	0.00	1.650E−13	20.0	99,800	4.021	20.3
HOL3-4	b9	20.41	1.8409	5.20	0.01	1.700E−14	11.8	92,235	9.763	100.7
HOL3-5	b8	50.29	1.4557	2.17	5.00	1.310E−13	16.6	126,162	2.354	17.7
HOL3-6	b9	27.09	1.0165	1.59	0.02	6.100E−14	6.6	76,476	2.254	88.2
HOL3-7	b9	50.95	1.8045	2.52	0.03	7.600E−14	9.2	82,166	2.742	16.9
blank b6	b6	n.a.	1.7321	1.81	0.02	7.600E−15	73.68	n.a.	n.a.	n.a.
blank b8	b8	n.a.	1.9069	1.94	0.00	0.000E+00	100.00	n.a.	n.a.	n.a.
blank b9	b9	n.a.	2.0149	2.04	0.01	2.000E−15	50.00	n.a.	n.a.	n.a

Table 4: Constants for age calculation (qtz: quartz; SLHL: sea level high latitude).

	constant/formula	reference
^{10}Be production rate SLHL	4.01±0.33 atoms/g qtz/a	Borchers et al. 2016
scaling		Stone 2000
^{10}Be mean-life (τ10) ^{10}Be half-life	2,001,018 a 1,387,000±12,000 a	Korschinek et al. 2010; Chmeleff et al. 2010
^{26}Al mean-life (τ26) ^{26}Al half-life	1,017,100 a 705,000±17,000 a	Nishiizumi 2004
effective burial mean-life	1/(1/τ26−1/τ10) 2,068,501 a	Granger 2014, Equ. 17; Erlanger et al. 2012, Equ. 4
production rate ratio ^{26}Al/^{10}Be	6.8±0.5	Nishizumii 1989; Zhao et al. 2016

weight ratio of 3.8±1.9 for detritus and ^{230}Th, ^{234}U and ^{238}U in secular equilibrium. All errors are given at the 2σ-level and include analytical uncertainties (i.e., counting statistics and mass spectrometric corrections, such as tailing, mass fractionation and ion-counter-to-Faraday cup amplification) as well as uncertainties in the spike calibration, the contribution of natural isotopes from the spike and the detrital correction (50 %). For a more detailed description of the calculation of the uncertainties, we refer the reader to Obert et al. (2018).

Luminescence dating

Samples were processed at the Vienna Laboratory for Luminescence dating (VLL). Samples for radionuclide measurement were first dried, aggregates were gently crushed by hand, and the bulk sample material was sealed in Marinelli beakers (500 ml, about 900 g dry weight). The beakers were stored for at least four weeks to establish secondary secular radon equilibrium. Luminescence samples were prepared under subdued red-light conditions. Those samples were opened and the outer few centimeters of material, which were exposed to daylight during sampling, were removed. The inner parts of the cores were removed from the tubes and used for all subsequent preparation steps. Separates of potassium-rich feldspar (150–200 µm) were extracted by standard laboratory techniques, including drying of the sediment at 50 °C, dry sieving, leaching of carbonates (10 % HCl) and organics (10 % H_2O_2), dispersion of aggregates and clay coatings ($Na_2C_2O_4$, 0.01 N), and density separation (LST Fastfloat at 2.58 g/cm^3, details in Lüthgens et al. 2017).

Quartz from the Vienna Basin area and the Eastern Alpine Foreland has repeatedly shown challenging properties for luminescence dating such as contribution of medium signal components to the bulk luminescence signal, low sensitivity, and feldspar contamination (e.g. Bickel et al. 2015a,b; Rades et al. 2018). We did not expect incomplete resetting of the luminescence signal before deposition due to the aeolian depositional environment and therefore used potassium-rich feldspar for all luminescence measurements, although it is bleached slower in nature compared to quartz. A post Infrared, Infrared stimulated SAR (single aliquot regenerative) protocol was applied, using stimulation temperatures of 50 °C and 225 °C, recording both the low temperature (IR50) and elevated temperature (pIRIR225) feldspar signals for subsequent equivalent dose determination (Buylaert et al. 2009, 2012; Bickel et al. 2015a,b; Lüthgens et al. 2017; Rades et al. 2018). Aliquots with a diameter of 1 mm (about 20 grains per aliquot) were prepared on stainless steel discs using silicone oil as adhesive. Samples were measured using a Risø DA-20 luminescence reader system (Bøtter-Jensen et al. 2000, 2003) using infrared (IR, 875 nm) LEDs for stimulation of the feldspar luminescence signal. The luminescence signal was recorded through a LOT/Oriel D410/30 optical interference filter, selecting the K-feldspar emission at 410 nm (Krbetschek et al. 1997). For laboratory irradiation, the luminescence reader delivers a doserate of approximately 0.1 Gy/s via a $^{90}Sr/^{90}Y$ beta source. Signals were integrated over the first second of the 100 s stimulation and the last 10 s were subtracted as background. Dose recovery experiments for each sample show good dose recovery within 5 % of unity, low recuperation (<5 % of the natural signal for IR50, <10 % for pIRIR225 indicating that no significant charge was carried over throughout SAR cycles), and good recycling within 5 % from unity for both signals. Fading (athermal signal loss over time, Wintle 1973) experiments were conducted using the approach of Auclair et al. (2003) but modified to also record the pIRIR225 signal. All tests verified that the applied pIRIR225 SAR protocol is suitable for the determination of the equivalent dose.

The natural radionuclide content of the samples was measured using a Canberra high resolution, low-level gamma spectrometer (high purity Ge detector, n-type, with an efficiency of 40 %) and a measurement time of at least 24 hours to gain an excellent signal to noise ratio. The overall doserate and ages were calculated using the software ADELE (Kulig 2005), with the cosmic doserate calculated according to Prescott & Stephan (1982) and Prescott & Hutton (1994) using conversion factors of Adamiec & Aitken (1998) and β-attenuation factors of Mejdahl (1979) for calculation of the external doserate. A low water content value of 10±5 %, was included in the calculations, because higher water content values seem unlikely to occur in a karstic drainage system. A potassium content of 12.5±0.5 % (Huntley & Baril 1997) and an a-value of 0.07±0.02 (Bickel et al. 2015a,b) were used for the calculation of the internal doserate.

Results

Sediment analysis

Granulometry of the cave sediment shows a wide size spectrum between >64 mm and 0.2 µm with a bimodal distribution. The pebble components (diameter >6.3 cm) consist mainly of quartz (97 %) and rarely quartzite (3 %). Matrix minerals are quartz, K-feldspar (microcline), muscovite, chlorite, clay minerals, and iron oxides (mainly hematite and amorphous iron oxides identified by STA). The clay fraction of samples HOL16/5A and 6A contain smectite, kaolinite and illite (Fig. 5). Smectite is identified by a broad peak at 14.3 Å with Mg saturation which shifts to 18.1 Å with Mg+ glycerol saturation. Saturation with K leads to a reduction of the interlayer spacing to 11.7 Å. After heating to 550 °C, smectite collapses to 9.9 Å. Illite is identified by the peaks at 9.9, 4.95, and 3.3 Å which do not shift during treatment. Kaolinite peaks at 7.13 and 3.57 Å disappear after heating to 550 °C. The clay mineral content is very similar for both samples and consists of 53–59 % smectite 25–33 % illite and 14–16 % kaolinite.

In contrast, the clay fraction from a sand lens (HOL16/3B) within a gravel body (see Fig. 4 and Table 1) contains jarosite and alunite in addition to illite, kaolinite, and smectite. The heavy mineral assemblage from this sand lens contains in the coarser fraction abundant tourmaline, kyanite, staurolite, epidote, sillimanite, less andalusite and rutile. The finer fraction additionally contains zircon and clinozoisite but no andalusite. No fossils were found during sample processing.

Burial age dating

Results from AMS measurements and calculation of nuclide concentrations of each sample are listed in Tables 3 and 4. Analogue to Braumann et al. (2019), the Peirce criterion

(Peirce 1852; Ross 2003) was applied to identify outliers. In that process, samples HOL3-6 and HOL3-7 were selected and excluded. As samples with a high measurement uncertainty such as samples HOL3-1, HOL3-4 and HOL3-6 are less robust, we excluded a total of 4 samples from age calculation.

The remaining data were used for isochron burial age calculation. A Monte Carlo simulation including the three remaining data points is shown in Fig. 6a and b, resulting in a mean age of 4.3±0.2 Ma based on 10,000 iterations from points randomly selected from within the measurement error. We note that within the large uncertainties, samples HOL3-4 would still plot on the isochron. To include potential variation in the production rate ratio in the source area (between 6.3 and 7.3, s. Table 1, adopted from Zhao et al. 2016) we additionally calculated ages using the highest and lowest starting ratio. The uncertainty of this range lies between 4.1 and 4.6 Ma and is therefore higher than the error of the original age calculated from a starting ratio of 6.8.

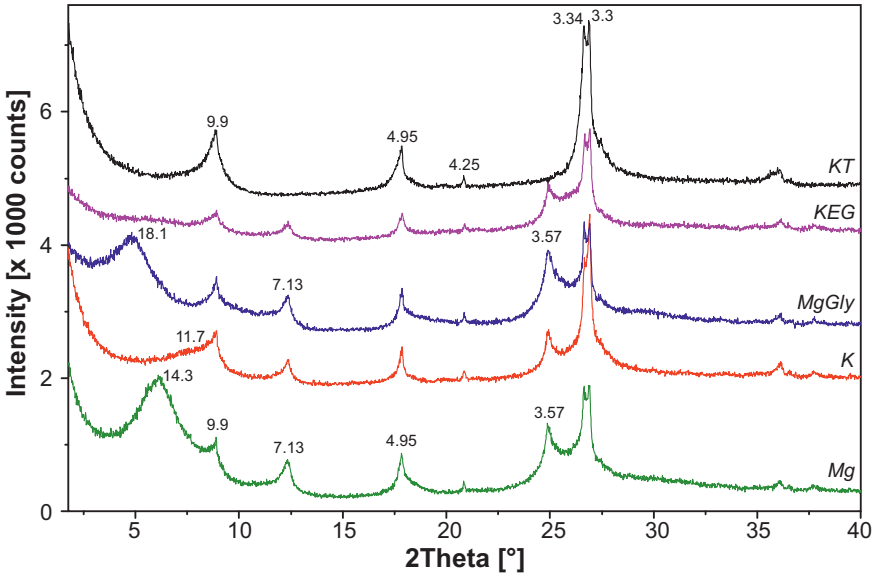

Fig. 5. X-ray patterns of the clay fraction of sample HOL16/5A, saturated with K, Mg, K and ethylene glycol (KEG), Mg and glycerol (MgGly) and heated to 550 °C (KT); d-values in Å.

^{230}Th/U-dating

Three cave raft samples were dated by the ^{230}Th/U-method; the results are presented in Table 5. The thin, sharp-edged, and uncoated cave raft (HH3-2) gave the youngest age of 322.7 +16/−14 ka. Samples from another niche to the left were slightly more overgrown (HH3-3, age 382.6 +41/−29) and samples from the inclined wall had quite a lot of coating (HH3-1, age 437.3 +39/−29).

Luminescence dating

All equivalent dose calculations, as well as fading correction used the R-luminescene package by Kreutzer et al. (2012). As expected from the results of the quality tests and the aeolian depositional environment, the equivalent dose measurements of both samples were highly reproducible, which is expressed in low overdispersion values of >7 % for all samples. Average equivalent doses were calculated for the IR50 and the pIRIR225 signal using the CAM (central age model, Galbraith et al. 1999). The results from gamma spectrometry did not show any indication of radionuclide disequilibria, and doserate calculations yielded similar overall doserates of c. 2.5 Gy/ka for both samples (Table 6). Fading tests yielded g values in the range of previous studies (Bickel et al. 2015a, b; Rades et al. 2018), averaging c. 2.8 for the IR50 signal and c. 1.2 for the pIRIR225 signal. The ages were fading corrected using the method of Huntley and Lamothe (2001). The fading corrected ages all agree within error (both, comparing individual samples and average ages of different luminescence signals), which proves the complete resetting of the luminescence signal. Incomplete resetting would result in a significant offset between IR50 ages and pIRIR225 ages, caused by the difference in bleachability of both signals (Murray et al. 2012). In summary, the luminescence ages reliably date the aeolian cover sediments to 14.6±1.0 ka (mean age ± standard deviation) and the identical results for IR50 and pIRIR225 ages confirm an aeolian transport.

Interpretation and discussion

Depositional setting

Field observations during several stages of quarrying gave a detailed three-dimensional picture of sediment bodies and their depositional environment to reconstruct the Plio- and Pleistocene geomorphological history of the Hainburg Hills area:

- **Formation of the chamber:** the sediment-filled cave chamber is significantly larger compared to other accessible caves in the Hollitzer quarry but its wall morphology is similar. Therefore, we assume that it formed hydrothermally under phreatic conditions (i.e. below the level of the Danube river). As this type of speleogenesis needs a thermal gradient it can be assumed that it occurred relatively close to the surface.
- **Paleoenvironmental conditions during the late Miocene:** A period of extensive soil formation under warm and humid conditions is documented by the presence of smectite, small amounts of mixed layer clays and hematite in the matrix. Those minerals precipitate authigenetically in the B-horizon

during pedogenesis as very fine-grained minerals (e.g. Churchman & Lowe 2012). This type of soil formation is also indicated by small grain sizes of <0.2 µm in matrix sample HOL16/3C. In addition, acidic soil conditions typical for (sub-) tropical soils are indicated by the presence of alunite and birnessite. Warm and humid climate results in a high rate of chemical weathering affecting unstable lithologies first and is inferred by the abundance of quartz clasts. In the field we observed weathered granite components that disintegrated during sieving. Lastly, the abundance of iron oxides, that are particularly enriched during lateritic soil genesis are typical for humid and warm climate typical for the late Miocene of the Pannonian Basin System (e.g. Utescher et al. 2017) and for the humid and warm conditions during the Early Pliocene (Böhme et al. 2011; Kovács et al. 2015).

- **Transport and deposition:** A large river transported and deposited gravel together with fine-grained soil-derived sediments above a Miocene rocky and karstified landscape. The dominance of quartz or quartzite in the gravel indicates intense chemical weathering of lithic components. In contrast, a sand lens (Fig. 3a) within the fluvial gravel contains heavy minerals that are easily dissolved during transport and weathering such as amphibole and tourmaline. This indicates short transport and exposure and has to be reconciled to the evidence from lithology of the coarse fraction. A plausible explanation could be that the coarse-grained stable lithologies (quartz and quartzite) and soil-derived fines were remobilized during floods where material is eroded and the river bank is affected by scouring. The fresh rock material from the sand lens most likely represents periods of average regimen.

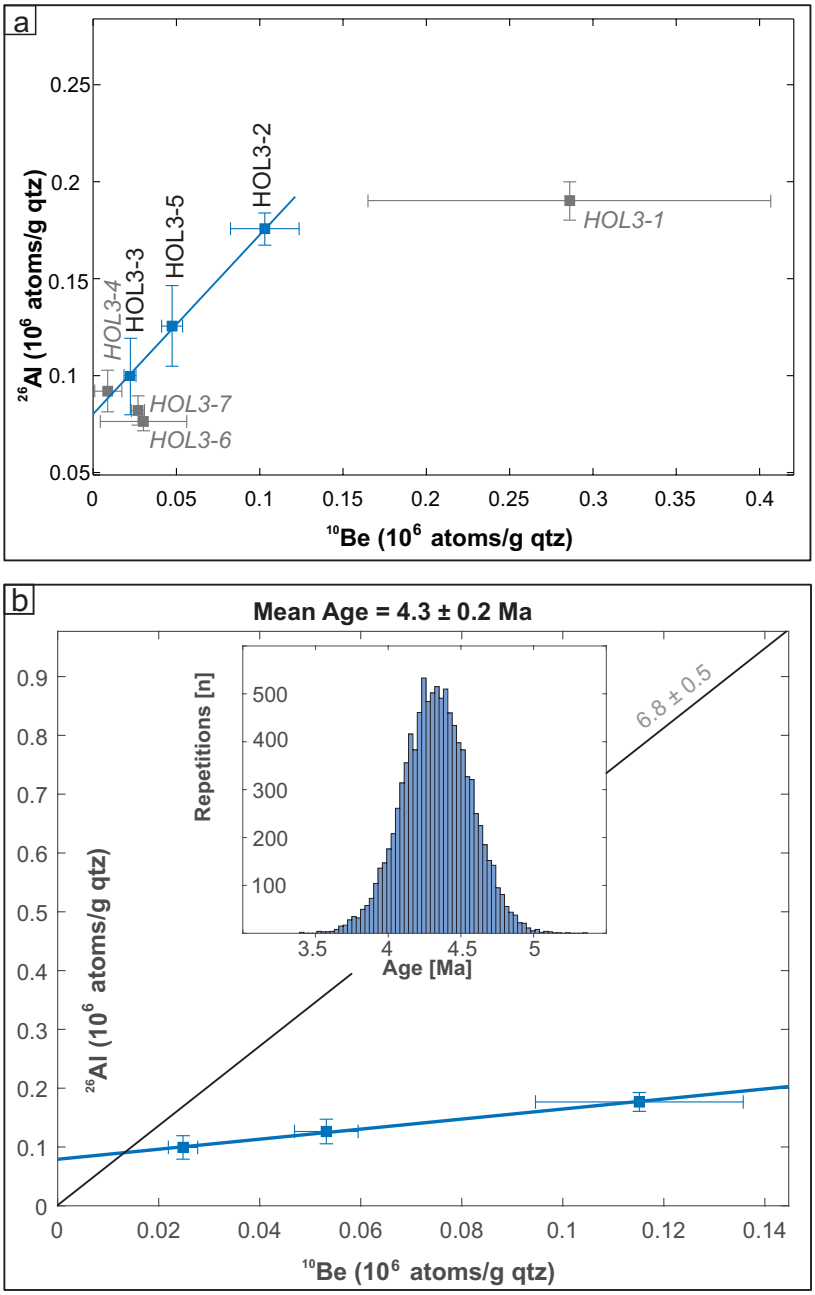

Fig. 6. a — ^{26}Al and ^{10}Be isotope distribution in all samples – grey samples not used for isochron calculation. **b** — Isochron diagram of all accepted HOL3 samples; inset: histogram of single run results of the Monte Carlo simulation for this specific isochron.

Table 5: Results of ^{230}Th/U-dating.

sample	^{238}U [µg/g]	±	^{232}Th [ng/g]	±	(^{234}U/^{238}U)	±	(^{230}Th/^{238}U)	±	age uncorr. [ka]	±	age corrected [ka]	±
HH3-1	1.1439	0.0068	14.27	0.15	1.0400	0.0017	1.0360	0.0057	437.6	+37/−28	**437.3**	**+39/−29**
HH3-2	1.4435	0.0088	7.441	0.094	1.0283	0.0017	0.9836	0.0073	322.8	+16/−14	**322.7**	**+16/−14**
HH3-3	1.2910	0.0086	28.86	0.39	1.0545	0.0030	1.0417	0.0098	383.2	+40/−30	**382.6**	**+41/−29**

Table 6: OSL data summary.

sample		depth (cm)	U^{238} (Bq/kg)[1]	Th^{232} (Bq/kg)[1]	K^{40} (Bq/kg)[1]	overall doserate (Gy/ka)[2]	n	D_e IR50 (Gy)[3]	D_e pIRIR225 (Gy)[3]	age IR50 faded (ka)[4]	age pIRIR225 faded (ka)[4]	g value IR50[5]	g value pIRIR225[5]	age IR50 fading corr. (ka)[6]	age pIRIR225 fading corr. (ka)[6]
laboratory code	field code														
VLL-0197-L	HOL1	50	24.5±0.6	23.8±0.7	323.1±7.1	2.6±0.2	6	26.4±0.9	33.4±1.0	10.2±0.7	12.9±0.9	2.8±0.2	1.1±0.3	13.3±1.0	14.2±1.1
VLL-0198-L	HOL2	50	23.1±0.6	21.1±0.6	299.4±6.5	2.4±0.2	6	28.2±0.7	34.7±0.6	11.5±0.8	14.2±0.9	2.8±0.2	1.4±0.2	15.0±1.1	16.1±1.1

[1] Radionuclide concentrations determined by high-resolution, low-level gamma spectrometry (Canberra n-type detector, c. 40 % efficiency).

[2] Overall environmental doserates calculated using 10±5 % water content and using conversion factors of Adamiec & Aitken (1998) and β-attenuation factors of Mejdahl (1979); cosmic doserate determined according to Prescott & Stephan (1982) and Prescott & Hutton (1994), including a potassium content of 12.5±0.5 % (Huntley & Baril 1997), an a-value of 0.07±0.02 (Bickel et al. 2015a, b).

[3] D_e calculated using the central age model (CAM) according to Galbraith et al. (1999) using the R Luminescence package (Kreutzer et al. 2012)

[4] Calculated using the software ADELE (Kulig 2005)

[5] Determined using the approach of Auclair et al. (2003), but modified to also include the pIRIR225 signal, using 6 aliquots for each sample.

[6] Fading correction using the stated g-values and the method of Huntley & Lamothe (2001)

- **Cave fill:** Shortly after deposition (in the order of a few thousand years), the fluvial gravels and soil-derived matrix were redeposited into the cave chamber when it was opened possibly by fluvial erosion or became unstable due to sediment overburden. The collapse is documented by the matrix support of the sediments in the cave and by the randomly oriented long axes of the cobbles. Thus, the numerical age calculated using the isochron method gives the timing of fluvial deposition at Danube's former base level (i.e. at the surface above the cave) and not the time of redeposition of the sediments into the cave.
- **Uplift:** Ongoing uplift/base level drop of the area of the Hainburg Hills lifted the gravel-filled cave chamber and sediments from fluvial influence and the lower HH3 cave reached a zone where cave rafts could form at the surface of the water.
- **Aeolian cover:** Deposition of fine aeolian sands in shallow karstic depressions and on the bedrock surface.

Dating and limits/uncertainties

For isochron dating four of seven clasts were excluded. One reason is analytical: batch 9 is problematic due to largely low currents resulting in high measurement uncertainty. This is caused by the small amount of carrier (equivalent to a mass of c. 150 µg Be) added to this batch and resulted in the exclusion of samples HOL3-1, HOL3-4 and HOL3-6. In comparison, samples from preceding batches 6 and 8 have a lower measurement uncertainty (Table 2).

Sample HOL3-7 does not follow a linear trend on the ^{10}Be versus ^{26}Al diagram, most likely due to inherited ^{10}Be (Fig. 6a). Outlier samples in isochron plots are to be expected, in particular in settings with multiple burial events previous to the last deposition. In samples with a long burial time in their previous deposit ^{26}Al is absent due to its faster decay and only ^{10}Be remains. When this clast re-enters the zone of nuclide production it still contains old (inherited) ^{10}Be and thus the ^{26}Al/^{10}Be ratio will be lower and plot under the isochron on the ^{10}Be vs ^{26}Al plot. These samples need to be excluded from age calculation. The remaining three samples form a linear regression of ^{10}Be versus ^{26}Al, that is used to calculate a central age of sediment deposition and burial at 4.3 Ma with an uncertainty of 0.2 Ma. As stated before, we note that sample HOL3-4 was excluded due to its large measurement error but it plots on the isochron-line. Monte Carlo runs of potential regression lines for this dataset are stronger influenced by the error of Al due to the flat slope of the regression line (s. Fig. 6b). Consequently, the overall error on the age is comparatively low. In summary, the uncertainty of this age including variation of the initial ^{26}Al/^{10}Be ratio (6.3–7.3, Zhao et al. 2016) lies between 4.1 and 4.6 Ma and agrees with results of the age range of 4.1–4.5 calculated from a starting ratio of 6.8. Uplift rates including the dating error as well as uncertainty in elevation of 10 m results in 36–42 m/Ma.

^{230}Th/U ages of the cave rafts from Hollitzerhöhle III (HH3, Fig. 7) are an order of magnitude younger than the burial ages

of the sediments and are located 58 m above the present Danube level, and 112 m below the position of the sediment dated by $^{26}Al/^{10}Be$ (165–175 m above the base of recent Danube sediments). Even though the rafts were collected from the same spot, one overgrown sample (HH3-1) is c. 100 ka older compared to pristine sample HH3-2. Therefore, the age calculated from the HH3-2 pristine raft most accurately represents the time of formation. Cave rafts form at the water surface, but their position in relation to the base level is unclear. Either they were formed in a hydrothermal karst aquifer at base level or at a local pool above the base level. Only in the first case, the age can be converted into an uplift/incision rate. In the second case, the age represents the time of local dry falling, and the computed uplift/incision rate calculated from the pristine sample HH3-2 of 150–162 m/Ma can only be considered as a maximum uplift rate.

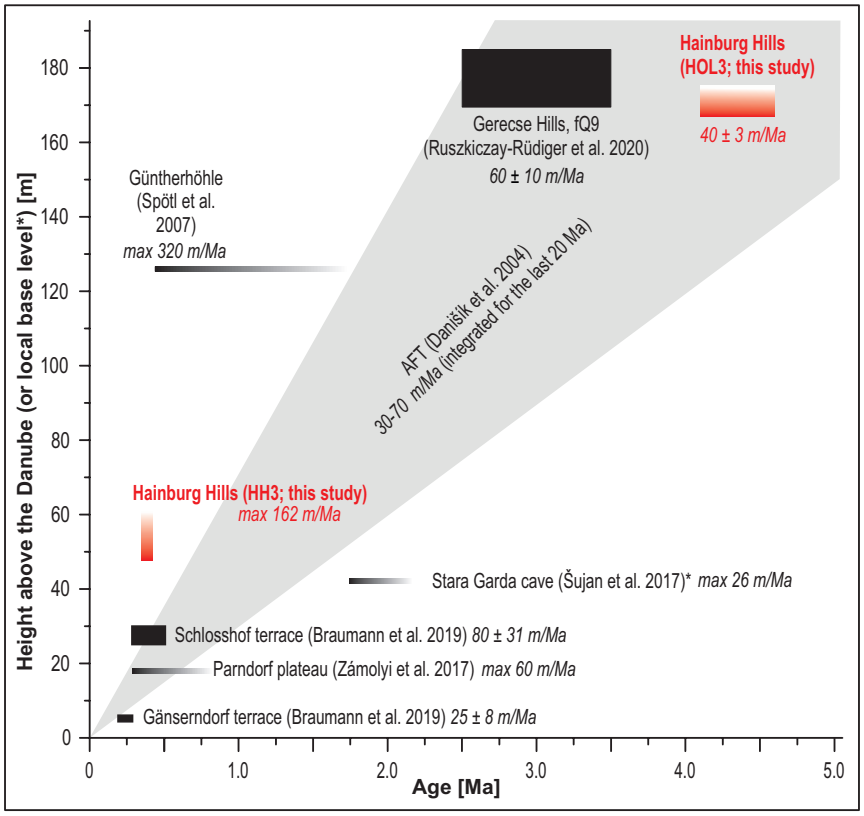

Fig. 7. Compilation of numerical uplift rates at the Alpine-Carpathian border. Shaded rectangles indicate a minimum age or maximum elevation (in the case of the calcite rafts) and might extend further in time/elevation.

Comparison of uplift/incision rates in the larger area

First, we compare the calculated ages and rates of base level drop to other studied sites in the region east of the Vienna Basin. Two more caves 1.4 km to the southeast of the study site (Fig. 2) provide minimum ages. Knochenspalte at 138 m above the Danube (270 m a.s.l.) is an unroofed cave that was completely filled with sediments and a rich fossil fauna from the early Middle Pleistocene onward (0.7 Ma; Frank & Rabeder 1997b). As the deposition of the sediment and bones is not fluvial, it occurred upslope of the base level and therefore gives a minimum age of uplift/base level drop. At the adjacent inactive hydrothermal cave "Güntherhöhle" a flowstone from the upper part 145 m above the Danube (277 m a.s.l.) was beyond the limit of the $^{230}Th/U$ method (at that time) and only a minimum age of 400 ka could be calculated (Spötl et al. 2007).

Data inferred from the crystalline basement north of the Hainburg Hills close to Devín (Danišík et al. 2004, their sample MK-16, s. Fig. 2) provide a long-term uplift rate of c. 30–70 m/Ma averaged for the last 20 Ma using apatite fission track dating. When comparing this number to the Hainburg Hills, it should be considered that this dataset integrates a five times longer timespan. Thus, a broad range is to be expected, however, the rate is in the same magnitude compared to the uplift/incision rate calculated for the Hainburg Hills.

The Stará Garda cave located in the Malé Karpaty Mts. north of the Danube and 22 km NE of the study area (Fig. 1) was investigated by $^{26}Al/^{10}Be$ burial age dating. Here, fine-grained quartz-rich sediments in the cave gave a minimum age of 1.72 Ma (Šujan et al. 2017). Fluvial transport today is influenced by a local creek c. 260 m above the Danube and hence the corresponding uplift rate is 26 m/Ma.

Zámolyi et al. (2017) dated terrace sediments from 20 km SSE of Hollitzer at the southern end of Parndorf Plateau to older than 0.3 Ma (Nickelsdorf, Fig. 1, their sample NIC 1). This can be converted into a change in base level of max. 60 m/Ma.

In the Vienna Basin, areas of sediment accumulation and uplift are juxtaposed and few data on terrace ages may be converted into uplift/incision rates. The Schlosshof terrace is located at the eastern border of the Vienna Basin close to the VBTFS and 12 km north of the Hollitzer quarry (Fig. 2). Here, the terrace age was constrained to 0.34±0.17 Ma at a height of 25–30 m above the base of the recent Danube channel. This can be converted into an uplift/incision rate of 80±31 m/Ma (Braumann et al. 2019). In comparison, the base of Gänserndorf Terrace 5–6 m above the Danube (Fig. 1) recorded gravel deposition at 0.24±0.05 Ma (Braumann et al. 2019) and documents an uplift/incision rate of 25±8 m/Ma.

At the eastern border of the Danube Basin, c. 100 km from the investigated location (Fig. 1) Ruszkiczay-Rüdiger et al. (2016, 2018, 2020) numerically dated the terrace record preserved in the eastern Danube Basin and western Transdanubian Range. In this area the average uplift/incision rate was gradually increasing from west to east, culminating in the Transdanubian Range between 50 and 70 m/Ma during the last ~3 Ma, integrated over a total of nine numerically dated terrace levels. However, this rate is slightly biased by the short-term fast incision during the last ~140 ka (207±1 m/Ma). The long-term uplift rate is suggested to be 51±5 m/Ma, a value derived from the terrace chronological data between ~3–0.3 Ma)

Comparing these rates to the wider area such as the Bohemian Massif or the Koralpe – both areas were unglaciated during the last ice ages – result in similar rates. For example, numerically undated Pleistocene fluvial gravels assigned to "Jüngere Deckenschotter" (Schnabel 2002) corresponding to Mindel (c. 0.4–0.5 Ma; van Husen & Reitner 2011) directly overlay crystalline Variscan rock at the southern edge of the Bohemian Massif. Their position tentatively documents uplift rates in the order of c. 50 m/Ma. At Koralple, basin wide denudation rates using ^{10}Be indicate an increase of erosion rates from ~40 m/Ma to ~140 m/Ma c. 4±1 Ma ago (Legrain et al. 2015).

In summary, uplift/incision rates calculated for the closer and larger unglaciated vicinity of the Hainburg Hills over the last 4.5 Ma range between a maximum of c. 150 m/Ma and a minimum of 20–25 m/Ma. The over-regional similarity of the uplift rates might point toward a thermal adjustment in the upper mantle or lower crust (Balázs et al. 2017; Ruzskiczay-Rüdiger 2020). In addition, increased erosion during the Pleistocene cooling period can influence the unroofing and enhance uplift (Kuhlemann et al. 2006). The interplay of deep lithospheric processes and erosion could be resolved in future geophysical models where the Hainburg Hills record contributes a boundary condition for the southernmost end of the Malé Karpaty Mts.

The average luminescence age of the cover sands of 14.6± 1.0 ka reveals two important features of landscape development in the research area. First, the cover sediments dating to the late MIS2 directly overlie gravels infilling the caves, which were dated to 4.1–4.6 Ma. This implies that erosional processes repeatedly removed any covering sediments deposited on top of the karstified bedrock surface, resulting in a gap in the stratigraphic record. In addition, the aeolian sediments are primarily preserved in depressions within the bedrock surface, which functioned as sediment traps. The luminescence age of the trapped sediments represents change of aeolian activity when sand transport and reworking stopped. The age of 14.6±1.0 ka for the termination of this phase may be correlated to other locations with aeolian deposits throughout Western and Central Europe documented around that time (e.g. Kasse 2002; Kasse et al. 2007; Vandenberghe et al. 2013). The ages also fall into the same age range determined for aeolian deposits in the Vienna Basin area (Schiefer et al. 2018), and for cover sediments from the eastern Danube Basin (Ruszkiczay-Rüdiger et al. 2016 – sample Ács-A1, Ács) and Transdanubian Range (Ruszkiczay-Rüdiger et al. 2018 – sample LUM 2283, Kender Hill).

Conclusion

Field evidence from the Hainburg Hills suggests the deposition of fluvial gravel from a large river – most likely the paleo-Danube – on top of a Paleozoic to Neogene succession. The gravel was mixed with red matrix containing smectite and alunite, minerals that indicate soil formation in a warm and humid climate. The sediments were trapped in near-surface cavities of Mesozoic limestones, which were karstified by hydrothermal waters and later opened towards the surface most probably by erosion and collapse. Fluvial sediments are in part covered by aeolian sands. The sediments record the ongoing uplift of the region as well as paleoclimatic change.

The timing of sediment deposition 165–175 m above the recent base of the Danube sediments was constrained to 4.1–4.6 Ma using ^{26}Al/^{10}Be isochron burial dating. The resulting change in base level over time corresponds to an uplift rate of 40±3 m/Ma and lies in a comparable range to rates reported for a similar timespan from unglaciated areas of the Eastern Alps and to the comprehensive terrace record at the Gerecse Hills of the Transdanubian Range.

Numerical ages from a pristine ^{230}Th/U cave raft 92 m below the sediment filled cave dated by ^{26}Al/^{10}Be document their formation ~0.33–0.16 Ma ago and record an increased rate of base level drop of 150–160 m/Ma for the time period between 0.3 Ma and today. Such an acceleration in uplift/incision has also been recorded for this time interval – roughly starting from the Middle Pleistocene – in sedimentary records from the Vienna Basin (Braumann et al. 2019) and the eastern Transdanubian Range (Ruszkiczay-Rüdiger et al. 2016, 2018). The joint geochronological and structural geological study in the latter setting revealed that the gradual acceleration of the incision rate during the Middle Pleistocene is most probably an artefact caused by integration over a short period of fast incision restricted to the last ~140 ka (Ruszkiczay-Rüdiger et al. 2020) and could be considered also for the situation presented in this study.

The aeolian cover deposits give an age of 14.6±1 ka and document a change in wind velocities at this time and an associated change to deposition of aeolian sediment most likely related to changes in the atmospheric circulation following the Last Glacial Maximum.

Acknowledgments: Godfried Wessely, Klemens Grösel, Gerlinde Posch-Trötzmüller and Eike Rades helped with fieldwork and detailed local expertise. Mr. Riegler and Mr. Bauer (Rohrdorfer company) enabled easy and multiple access to the Hollitzer quarry. Philipp Strauss contributed his expertise for the section (Fig. 1b). Peter Steier is thanked for laboratory support regarding preparation of AMS targets and AMS analysis. S. Neuhuber thanks D. Schaferl for laboratory support

and M. Hirsch for OES analyses. D. Scholz acknowledges funding of the German Research Foundation (DFG SCHO 1274/9-1 and DFG SCHO 1274/11-1). In addition, D. Scholz is thankful to K.P. Jochum, M.O. Andreae and G.H. Haug from the Max Planck Institute for Chemistry, Mainz, Germany, for their long-lasting support. The thorough and constructive reviews of J. Minár, Zs. Ruszkiczay-Rüdiger and M. Šujan improved the manuscript substantially. The project was financed by Hochschuljubiläumsstiftung der Stadt Wien (H-2899959_2016).

References

Adamiec G. & Aitken M. 1998: Dose-rate conversion factors: update. *Ancient TL* 16, 37–50.

Akhmadaliev S., Heller R., Hanf D., Rugel G. & Merchel S. 2013: The new 6 MV AMS-facility DREAMS at Dresden. *Nuclear Instruments and Methods in Physics Research Section B: Beam Interactions with Materials and Atoms* 294, 5–10. https://doi.org/10.1016/j.nimb.2012.01.053

Auclair M., Lamothe M. & Huot S. 2003: Measurement of anomalous fading for feldspar IRSL using SAR. *Radiation Measurements* 37, 487–492. https://doi.org/10.1016/S1350-4487(03)00018-0

Balázs A., Burov, E., Matenco L., Vogt, K., Francois T. & Cloetingh S. 2017: Symmetry during the syn- and post-rift evolution of extensional back-arc basins: the role of inherited orogenic structures. *Earth and Planetary Science Letters* 462, 86–98. https://doi.org/10.1016/j.epsl.2017.01.015

Balco G. & Rovey C.W. II 2008: An isochron method for cosmogenic-nuclide dating of buried soils and sediments. *American Journal of Science* 308, 1083–1114. https://doi.org/10.2475/10.2008.02

Bella P., Bosák P., Braucher R., Pruner P., Hercman H., Minár J., Veselský M., Holec J. & Léanni L. 2019: Multi-level Domica–Baradla cave system (Slovakia, Hungary): Middle Pliocene–Pleistocene evolution and implications for the denudation chronology of the Western Carpathians. *Geomorphology* 327, 62–79. https://doi.org/10.1016/j.geomorph.2018.10.002

Bickel L., Lüthgens C., Lomax J. & Fiebig M. 2015a: Luminescence dating of glaciofluvial deposits linked to the penultimate glaciation in the Eastern Alps. *Quaternary International* 357, 110–124. https://doi.org/10.1016/j.quaint.2014.10.013

Bickel L., Lüthgens C., Lomax J. & Fiebig M. 2015b: The timing of the penultimate glaciation in the northern Alpine Foreland: new insights from luminescence dating. *Proceedings of the Geologists' Association* 126, 536–550. https://doi.org/10.1016/j.pgeola.2015.08.002

Böhme M., Winklhofer M. & Ilg A. 2011: Miocene precipitation in Europe: Temporal trends and spatial gradients. *Paleogeography, Paleoclimatology, Paleoecology* 304, 212–218. https://doi.org/10.1016/j.palaeo.2010.09.028

Borchers B., Marrero S., Balco G., Caffee M., Goehring B., Lifton N., Nishiizumi K., Phillips F., Schaefer J. & Stone J. 2016: Geological calibration of spallation production rates in the CRONUS-Earth project. *Quaternary Geochronology* 31 188–198. https://doi.org/10.1016/j.quageo.2015.01.009

Bøtter-Jensen L., Andersen C., Duller G. & Murray A. 2003: Developments in radiation, stimulation and observation facilities in luminescence measurements. *Radiation Measurements* 37, 535–541. https://doi.org/10.1016/S1350-4487(03)00020-9

Bøtter-Jensen L., Bulur E., Duller G. & Murray A. 2000: Advances in luminescence instrument systems. *Radiation Measurements* 32, 523–528. https://doi.org/10.1016/S1350-4487(00)00039-1

Braucher R., Bourlès D., Merchel S., Vidal Romani J., Fernadez-Mosquera D., Marti K. & Keddadouche K. 2013: Determination of muon attenuation lengths in depth profiles from in situ produced cosmogenic nuclides. *Nuclear Instruments and Methods in Physics Research Section B: Beam Interactions with Materials and Atoms* 294, 484–490. https://doi.org/10.1016/j.nimb.2012.05.023

Braumann S.M., Neuhuber S., Fiebig M., Schaefer J.M. & Lüthgens C. 2019: Challenges in constraining ages of fluvial terraces in the Vienna Basin (Austria) using combined isochron burial and pIRIR225 luminescence dating. *Quaternary International* 509, 87–102. https://doi.org/10.1016/j.quaint.2018.01.009

Buylaert J., Murray A., Thomsen K. & Jain M. 2009: Testing the potential of an elevated temperature IRSL signal from K-feldspar. *Radiation Measurements* 44, 560–565. https://doi.org/10.1016/j.radmeas.2009.02.007

Buylaert J., Jain M., Murray A., Thomsen K., Thiel C. & Sohbati R. 2012: A robust feldspar luminescence dating method for Middle and Late Pleistocene sediments. *Boreas* 41, 435–451. https://doi.org/10.1111/j.1502-3885.2012.00248.x

Cheng H., Edwards R.L., Hoff J., Gallup C.D., Richards D.A. & Asmerom Y. 2000: The half-lives of uranium-234 and thorium-230. *Chemical Geology* 169, 17–33. https://doi.org/10.1016/S0009-2541(99)00157-6

Chmeleff J., von Blanckenburg F., Kossert K. & Jakob D. 2010: Determination of the ^{10}Be half-life by multicollector ICP-MS and liquid scintillation counting. *Nuclear Instruments and Methods in Physics Research Section B: Beam Interactions with Materials and Atoms* 268, 192–199. https://doi.org/10.1016/j.nimb.2009.09.012

Churchman G.J. & Lowe D.J. 2012: Alteration, formation, and occurrence of minerals in soils. In: Huang P.M., Li Y. & Sumner M.E. (Eds.): Handbook of Soil Sciences. 2nd edition, Vol. 1: Properties and Processes. *CRC Press (Taylor & Francis)*, Boca Raton, FL, 20.1–20.72.

Cohen K.M., Finney S.C., Gibbard P.L. & Fan J.-X. (2013; updated): The ICS International Chronostratigraphic Chart. *Episodes* 36, 199–204. https://doi.org/10.18814/epiiugs/2013/v36i3/002

Danišik M., Dunkl I., Putiš M., Frisch W. & Kráľ J. 2004: Tertiary burial and exhumation history of basement highs along the NW margin of the Pannonian Basin-an apatite fission track study. *Austrian Journal of Earth Sciences* 95–96, 60–70.

De Waele J., Audra P., Madonia G., Vattano M., Plan L., D'Angeli I.M., Bigot J.Y. & Nobécourt J.C. 2016: Sulfuric acid speleogenesis (SAS) close to the water table: Examples from southern France, Austria, and Sicily. *Geomorphology* 253, 452–467. https://doi.org/10.1016/j.geomorph.2015.10.019

Erlanger E.D., Granger D.E. & Gibbon R.J. 2012: Rock uplift rates in South Africa from isochron burial dating of fluvial and marine terraces. *Geology* 40, 1019–1022. https://doi.org/10.1130/G33172.1

Frank C. & Rabeder G. 1997a: Deutsch-Altenburg. In: Döppes D. & Rabeder G. (Eds.): Pliozäne und pleistozäne Faunen Österreichs. Ein Katalog der wichtigsten Fossilfundstellen und ihrer Faunen. *Mitteilungen der Kommission für Quartärforschung der Österreichischen Akademie der Wissenschaften* 10, 238–240.

Frank C. & Rabeder G. 1997b: Hundsheim. In: Döppes D. & Rabeder G. (Eds.): Pliozäne und pleistozäne Faunen Österreichs. Ein Katalog der wichtigsten Fossilfundstellen und ihrer Faunen. *Mitteilungen der Kommission für Quartärforschung der Österreichischen Akademie der Wissenschaften* 10, 270–274.

Fuchs W. 1986a: Geologische Karte der Republik Österreich 1:50.000. 61 Hainburg an der Donau-62 Pressburg. *Geologische Bundesanstalt*, Wien.

Fuchs W. 1986b: Geologische Karte der Republik Österreich 1:50.000. 60 Bruck an der Leitha. *Geologische Bundesanstalt*, Wien.

Galbraith R., Roberts R., Laslett G., Yoshida H. & Olley J. 1999: Optical dating of single and multiple grains of Quartz from Jinmium rock shelter, northern Australia: Part I, experimental design and statistical models. *Archaeometry* 41, 339–364. https://doi.org/10.1111/j.1475-4754.1999.tb00987.x

Garcia-Ibaibarriaga N. Arrizabalaga A., Iriarte-Chiapusso M-J, Rofes J. & Murealga X. 2015: The return of the Iberian Peninsula: first Quaternary record of *Muscardinus* and a palaeogeographical overview of the genus in Europe. *Quaternary Science Reviews* 119, 106–115. https://doi.org/10.1016/j.quascirev.2015.04.017

Gibbon R.J., Granger D.E., Kuman K. & Partridge T.C. 2009: Early Acheulean technology in the Vaal River Gravels, South Africa, dated with cosmogenic nuclides. *Journal of Human Evolution* 56, 152–160. https://doi.org/10.1016/j.jhevol.2008.09.006

Gibert L., Scott G.R., Scholz D., Budsky A., Ferrandez C., Martin R.A., Ribot F. & Leria M. 2016: Chronology for the Cueva Victoria fossil site (SE Spain): Evidence for Early Pleistocene Afro–Iberian dispersals. *Journal of Human Evolution* 90, 183–197. https://doi.org/10.1016/j.jhevol.2015.08.002

Granger D.E. 2014: Cosmogenic nuclide burial dating in archaeology and paleoanthropology. In: Holland H.D. & Turekian K.K. (Eds.): Treatise on Geochemistry. *Elsevier*, Oxford, 81–97.

Granger D.E. & Fabel D. 2019: Dating cave sediments with cosmogenic nuclides. In: White W., Culver D. & Pipan T. (Eds.): Encyclopedia of Caves (Third Edition). *Academic Press*, Cambridge, 348–352. https://doi.org/10.1016/B978-0-12-814124-3.00038-8

Granger D.E., Fabel D. & Palmer A.N. 2001: Pliocene–Pleistocene incision of the Green River, Kentucky, determined from radioactive decay of cosmogenic ^{26}Al and ^{10}Be in Mammoth Cave sediments. *Geological Society of America Bulletin* 113, 825–836. https://doi.org/10.1130/0016-7606(2001)113<0825:PPIOTG>2.0.CO;2

Haeuselmann P., Granger D.E., Jeannin P-Y. & Lauritzen S.E 2007: Abrupt glacial valley incision at 0.8 Ma dated from cave deposits in Switzerland. *Geology* 35, 143–146. https://doi.org/10.1130/G2309A.1

Halouzka R. & Minařiková D. 1977: Stratigraphic correlation of Pleistocene deposits of the river Danube in the Vienna and Komarno Basin. *Sborník geologických věd, Antropozoikum* 11, 7–55.

Hill C. & Forti P. 1997: Cave minerals of the world. *National Speleological Society*, Huntsville, 1–463.

Huntley D. & Baril M. 1997: The K content of the K-feldspars being measured in optical and thermoluminescence dating. *Ancient TL* 15, 11–13.

Huntley D. & Lamothe M. 2001: Ubiquity of anomalous fading in K-feldspars and the measurement and correction for it in optical dating. *Canadian Journal of Earth Sciences* 38, 1093–1106. https://doi.org/10.1139/e01-013

Kasse C. 2002: Sandy aeolian deposits and environments and their relation to climate during the Last Glacial Maximum and Lateglacial in northwest and central Europe. *Progress in Physical Geography* 26, 507–532. https://doi.org/10.1191/0309133302pp350ra

Kasse C., Vandenberghe D., de Corte F. & van den Haute P. 2007: Late Weichselian fluvio-aeolian sands and coversands of the type locality Grubbenvorst (southern Netherlands): Sedimentary environments, climate record and age. *Journal of Quaternary Science* 22, 695–708. https://doi.org/10.1002/jqs.1087

Kovács J., Szabó P., Kocsis L., Vennemann T., Sabol M., Gasparik M. & Virág A. 2015: Pliocene and Early Pleistocene paleoenvironmental conditions in the Pannonian Basin (Hungary, Slovakia): Stable isotope analyses of fossil probiscidean and perissodactyl teeth. *Paleogeography, Paleoclimatology, Paleoecology* 440, 455–466. https://doi.org/10.1016/j.palaeo.2015.09.019

Korschinek G., Bergmaier A., Faestermann T., Gerstmann U.C., Knie K., Rugel G. & Kossert K. 2010: A new value for the half-life of ^{10}Be by heavy-ion elastic recoil detection and liquid scintillation counting. *Nuclear Instruments and Methods in Physics Research Section B: Beam Interactions with Materials and Atoms* 268, 187–191. https://doi.org/10.1016/j.nimb.2009.09.020

Köster E. 1964: Granulometrische und morphometrische Messmethoden an Mineralkörnern, Steinen und sonstigen Stoffen. *Ferdinand Enke,* Stuttgart, 1–336.

Krbetschek M., Götze J. & Dietrich A. 1997: Spectral information from minerals relevant for luminescence dating. *Radiation Measurements* 32, 695–748. https://doi.org/10.1016/S1350-4487(97)00223-0

Kreutzer S., Schmidt C., Fuchs M., Dietze M. & Fuchs M. 2012: Introducing an R package for luminescence dating analysis. *Ancient TL* 30, 1–8.

Kuhlemann J., Dunkl I., Brügel A., Spiegel C. & Frisch W. 2006: From source terrains of the Eastern Alps to the Molasse Basin: Detrital record of non-steady-state exhumation. *Tectonophysics* 413, 301–316. https://doi.org/10.1016/j.tecto.2005.11.007

Kulig G. 2005: Erstellung einer Auswertesoftware zur Altersbestimmung mittels Lumineszenzverfahren unter spezieller Berücksichtigung des Einflusses radioaktiver Ungleichgewichte in der ^{238}U-Zerfallsreihe. *B.Sc. Thesis*, *Technische Universität Bergakademie Freiberg*, Freiberg, 1–35.

Legrain N., Dixon J., Stüwe K., von Blanckenburg F., & Kubik P. 2015: Post-Miocene landscape rejuvenation at the eastern end of the Alps. *Lithosphere* 7, 3–13. https://doi.org/10.1130/L391.1

Lüthgens C., Neuhuber S., Grupe S., Payer T., Peresson M. & Fiebig M. 2017: Geochronological investigations using a combination of luminescence and cosmogenic nuclide burial dating of drill cores from the Vienna Basin. *Zeitschrift der Deutschen Gesellschaft für Geowissenschaften* 168, 115–140. https://doi.org/10.1127/zdgg/2017/0081

Mais K. & Rabeder G. 1977: Eine pliozäne Höhlenfüllung im Pfaffenberg bei Bad Deutsch-Altenburg (Niederösterreich). *Die Höhle* 28, 1–7.

Maul L.C. & Markova A.K. 2007: Similarity and regional differences in Quarternary arvicolid evolution in Central and Eastern Europe. *Quaternary International* 160, 81–99.

Mejdahl V. 1979: Thermoluminescence dating: beta attenuation in quartz grains. *Achaeometry* 21, 61–73. https://doi.org/10.1111/j.1475-4754.1979.tb00241.x

Moore D.M. & Reynolds R.C.Jr. 1997: X-ray diffraction and the identification and analysis of clay minerals. *Oxford University Press*, New York, 1–378.

Murray A., Thomsen K., Masuda N., Buylaert J. & Jain M. 2012: Identifying well-bleached quartz using the different bleaching rates of quartz and feldspar luminescence signals. *Radiation Measurements* 47, 688–695. https://doi.org/10.1016/j.radmeas.2012.05.006

Nadachowski A., Stefaniak K., Szynkiewicz A., Marciszak A., Socha P., Schick P. & Czeslaw A. 2011: Biostraitgraphic importance of the Early Pleistocene fauna from Żabia Cave (Poland) in Central Europe. *Quarternary International* 243, 204–218.

Nishiizumi K. 2004: Preparation of Al-26 AMS standards. *Nuclear Instruments and Methods in Physics Research Section B: Beam Interactions with Materials and Atoms* 223, 388–392. https://doi.org/10.1016/j.nimb.2004.04.075

Obert J.C., Scholz D., Felis T., Brocas W., Jochum K.P. & Andreae M.O. 2016: ^{230}Th/U dating of Last Interglacial brain corals from Bonaire (southern Caribbean) using bulk and theca wall material. *Geochimica et Cosmochimica Acta* 178, 20–40. https://doi.org/10.1016/j.gca.2016.01.011

Obert J.C., Scholz D., Lippold J., Felis T., Jochum K.P. & Andreae M.O. 2018: Chemical separation and MC-ICPMS analysis of U, Th, Pa and Ra isotope ratios of carbonates. *Journal of Analytical Atomic Spectrometry* 33, 1372–1383. https://doi.org/10.1039/C7JA00431A

Peirce B. 1852: Criterion for the rejection of doubtful observations. *Astronomical Journal* 2, 161–163.

Plan L. 2019: Neue Höhlen im Steinbruch Hollitzer bei Bad Deutsch-Altenburg. - *Höhlenkundliche Mitteilungen Wien* 75, 157–164.

Plan L. & Spötl C. 2016: Hypogene Karsthöhlen. In: Spötl C., Plan L. & Christian E. (Eds.): Höhlen und Karst in Österreich. *OÖ-Landesmuseum,* Linz, 49–60.

Prescott J. & Hutton J. 1994: Cosmic ray distributions to dose rates for luminescence and ESR dating: large depths and long-term variations. *Radiation Measurements* 23, 497–500. https://doi.org/10.1016/1350-4487(94)90086-8

Prescott J. & Stephan L. 1982: The contribution of cosmic radiation to the environmental dose for thermoluminescent dating – Latitude, altitude and depth dependencies. *PACT* 6, 17–25.

Preusser F., Degering D., Fuchs M., Hilgers A., Kadereit A., Klasen N., Krbetschek M., Richter D. & Spencer J. 2008: Luminescence dating: basics, methods and applications. *E&G Quaternary Science Journal* 57, 95–149. https://doi.org/10.3285/eg.57.1-2.5

Rades E., Fiebig M. & Lüthgens C. 2018: Luminescence dating of the Rissian type section in southern Germany as a base for correlation. *Quaternary International* 478, 38–50. https://doi.org/10.1016/j.quaint.2016.07.055

Rhodes E. 2011: Optically Stimulated Luminescence Dating of Sediments over the Past 200,000 Years. *Annual Review of Earth and Planetary Sciences* 39, 461–488. https://doi.org/10.1146/annurev-earth-040610-133425

Ross S.M. 2003: Peirce's criterion for the elimination of suspect experimental data. *Journal of Engineering Technology* 20, 38–41.

Ruszkiczay-Rüdiger Zs., Braucher R., Novothny Á., Csillag G., Fodor L., Molnár G., Madarász B. & ASTER Team 2016: Tectonic and climatic forcing on terrace formation: coupling in situ produced ^{10}Be depth profiles and luminescence approach, Danube River, Hungary, Central Europe. *Quaternary Science Reviews* 131, 127–147. https://doi.org/10.1016/j.quascirev.2015.10.041

Ruszkiczay-Rüdiger Zs., Csillag G., Fodor L., Braucher R., Novothny Á., Thamó-Bozsó E., Virág A., Pazonyi P., Timár G., Aumâtre D., Burlés D. & Keddadouche K. 2018: Integration of new and revised chronological data to constrain the terrace evolution of the Danube River (Gerecse Hills, Pannonian Basin). *Quarternary Geochronolgy* 48, 148–170. https://doi.org/10.1016/j.quageo.2018.08.003

Ruszkiczay-Rüdiger Zs., Balázs A., Csillag G., Drijkoningen G. & Fodor L. 2020: Uplift of the Transdanubian Range, Pannonian Basin: How fast and why? *Global and Planetary Change* 192 103263. https://doi.org/10.1016/j.gloplacha.2020.103263

Salcher B.C., Meurers B., Smit J., Decker K., Hölzel M. & Wagreich M. 2012: Strike-slip tectonics and Quaternary basin formation along the Vienna Basin fault system inferred from Bouguer gravity derivatives. *Tectonics* 31,1–20. https://doi.org/10.1029/2011TC002979

Schiefer J., Lair G., Lüthgens C., Wild E., Steier P., Blum W. 2018: The increase of soil organic carbon as proposed by the "4/1000 initiative" is strongly limited by the status of soil development – A case study along a substrate age gradient in Central Europe. *Science Of The Total Environment* 628–629, 840–847. https://doi.org/10.1016/j.scitotenv.2018.02.008

Schnabel W. 2002: Geologische Karte von Niederösterreich 1:200 000. *Geologische Bundesanstalt,* Wien.

Scholz D. & Hoffmann D.L. 2008: ^{230}Th/U-dating of fossil reef corals and speleothems. *E&G Quaternary Science Journal* 57, 52–77. https://doi.org/10.3285/eg.57.1-2.3

Schultz L.G. 1964: Quantitative interpretation of mineralogical composition from X-ray and chemical data for the Pierre shale. *US Geological Survey Professional Paper* 391–C, 1–31.

Spötl C., Offenbecher K.H., Boch R., Meyer M., Mangini A., Kramers J. & Pavuza R. 2007: Tropfstein-Forschung in österreichischen Höhlen – ein Überblick. *Jahrbuch der Geologischen Bundesanstalt* 147, 117–167.

Spötl C., Plan L. & Dublyansky Y. 2017: Hypogene Karst in Austria. In: Klimchouk A., Palmer A.N., De Waele J., Auler A. & Audra P. (Eds.): Hypogene Karst Regions and Caves of the World. *Springer,* New York, 113–126.

Steier P., Martschini M., Buchriegler J., Feige J., Lachner J., Merchel S., Michlmayr L., Priller A., Rugel G., Schmidt E., Wallner A., Wild E.M. & Golser R. 2019: Comparison of methods for the detection of ^{10}Be with AMS and a new approach based on a silicon nitride foil stack. *International Journal of Mass Spectrometry* 444, 116–175. https://doi.org/10.1016/j.ijms.2019.116175

Stone J.O. 1998: A rapid fusion method for separation of Beryllium-10 from soils and silicates. *Geochimica et Cosmochimica Acta* 62, 555–561. https://doi.org/10.1016/S0016-7037(97)00340-2

Stone J.O. 2000: Air pressure and cosmogenic isotope production. *Journal of Geophysical Research* 105, B10, 23753–23759. https://doi.org/10.1029/2000JB900181

Strauss P., Harzhauser M., Hinsch R. & Wagreich M. 2006: Sequence stratigraphy in a classic pull-apart basin (Neogene, Vienna Basin). A 3D seismic based approach. *Geologica Carpathica* 57, 185–197.

Šujan M., Lačný A., Braucher R., Magdolen P., ASTER Team 2017: Early Pleistocene age of fluvial sediment in the Stará Garda Cave revealed by ^{26}Al/^{10}Be burial dating: impilication for geomorphic evolution of the Malé Karpaty Mts. (Western Carpathians). *Acta Carsologica* 46, 251–264. https://doi.org/10.3986/ac.v46i2-3.5157

Šujan M., Braucher R., Rybár S., Maglay J., Nagy A., Fordinál K., Šarinová K., Sýkora M., Józsa Š., ASTER Team & Kováč M. 2018: Revealing the late Pliocene to Middle Pleistocene alluvial archive in the confluence of the Western Carpathian and Eastern Alpine rivers: ^{26}Al/^{10}Be burial dating from the Danube Basin (Slovakia). *Sedimentary Geology* 377, 131–146. https://doi.org/10.1016/j.sedgeo.2018.10.001

Szanyi Gy., Surányi G. & Leél-Össy Sz. 2012: Cave development and Quaternary uplift history in the Central Pannoian Basin derived from speleothem ages. *Quaternary Geochronology* 14, 18–25. https://doi.org/10.1016/j.quageo.2012.09.001

Sztanó O., Kováč M., Magyar I., Šujan M., Fodor L., Uhrin A., Rybár S., Csillag G. & Tőkés L. 2016: Late Miocene sedimentary record of the Danube/Kisalföld Basin: interregional correlation of depositional systems, stratigraphy and structural evolution. *Geologica Carpathica* 67, 525–542. https://doi.org/10.1515/geoca-2016-0033

Uetscher T., Erdei B., Hably L. & Mosbrugger V. 2017: Late Miocene vegetation of the Pannonian Basin. *Palaeogeography, Palaeoclimatology, Paleoecology* 467, 131–148. https://doi.org/10.1016/j.palaeo.2016.02.042

Uher P., Kohút M., Ondrejka M., Konečný P. & Siman P. 2014: Monazite-(Ce) in Hercynian granites and pegmatites of the Bratislava Massif, Western Carpathians: compositional variations and Th–U–Pb electron-microprobe dating. *Acta Geologica Slovaca* 6, 215–231.

Vandenberghe D., Derese C., Kasse C. & Van den Haute P. 2013: Late Weichselian fluvio-aeolian sediments and Holocene drift-sands of the classic type locality in Twente (E Netherlands): a high-resolution dating study using optically stimulated luminescence. *Quaternary Science Reviews* 68, 93–113. https://doi.org/10.1016/j.quascirev.2013.02.009

van Husen D. & Reitner J. M. 2011: An outline of the Quaternary Stratigraphy of Austria. *Quarternary Science Journal* 60, 366–387.

Wallner A., Iked Y., Kutschera W., Priller A., Steier P. Vonach H. & Wild E. 2000: Precision and accuracy of ^{26}Al measurements at VERA. *Nuclear Instruments and Methods in Physics Research Section B: Beam Interactions with Materials and Atoms* 172, 1–4, 382–38. https://doi.org/10.1016/S0168-583X(00)00136-1

Wessely G. 1961: Geologie der Hainburger Berge. *Jahrbuch der Geologischen Bundesanstalt* 104, 273–349.

Wessely G. 2006: Geologie der Österreichischen Bundesländer: Niederösterreich. *Geologische Bundesanstalt,* Wien, 1–377.

Wintle A. 1973: Anomalous Fading of Thermo-luminescence in Mineral Samples. *Nature* 245, 143–144. https://doi.org/10.1038/245143a0

Wintle A. 2008: Luminescence dating: where it has been and where it is going. *Boreas* 37, 471–482. https://doi.org/10.1111/j.1502-3885.2008.00059.x

Yang Q., Scholz D., Jochum K.P., Hoffmann D.L., Stoll B., Weis U., Schwager B. & Andreae M.O. 2015: Lead isotope variability in speleothems – A promising new proxy for hydrological change? First results from a stalagmite from western Germany. *Chemical Geology* 396, 143–151. https://doi.org/10.1016/j.chemgeo.2014.12.028

Zámolyi A., Salcher B., Draganits E., Exner U., Wagreich M. Gier, S. Fiebig M., Lomax J., Surányi G., Diel M. & Zámolyi F. 2017: Latest Pannonian and Quaternary evolution at the transition between Eastern Alps and Pannonian Basin: new insights from geophysical, sedimentological and geochronological data. *International Journal of Earth Sciences* 106, 1695–1721. https://doi.org/10.1007/s00531-016-1383-3

Zhao Z., Granger, D., Zhang, M., Kong, X., Yang, S., Chen, Y. & Hu E. 2016: A test of the isochron burial dating method on fluvial gravels within the Pulu volcanic sequence, West Kunlun Mountains, China. *Quaternary Geochronology* 34, 75–80. https://doi.org/10.1016/j.quageo.2016.04.003

Zottl H. & Erber H. 2003: Donau östlich von Wien, Flussbauliches Gesamtprojekt. *UVE, Im Auftrag von via donau*, 1–56 (Project report in German).